Novel two-step synthesis of delafossite $CuFeO_2$ photocathodes for water splitting

Master Thesis

Yannick Geertzema, BSc

March 23, 2018

Supervisors:
Prof. Dr. Ir. B.M. Weckhuysen
Dr. F. Meirer
I. Garcia Torregrosa MSc

Inorganic Chemistry & Catalysis
University of Utrecht
The Netherlands

Contents

Chapter 1

Introduction

Ever since the industrial revolution took place in the 18th century, vast amounts of fossil fuels have been used to produce electricity, heat buildings and power all means of transportation. With the combustion of those fossil fuels enormous amounts of carbon dioxide, methane and other greenhouse gasses have been emitted in Earth's atmosphere, thereby damaging the ozone layer and severely increasing the average temperature on Earth. As an effect climate is changing around the globe, ice caps are melting and the sea level is rising. In order to slow down and eventually stop this climate change scientist have been investigating different, and most importantly, renewable energy sources. New energy sources like blue energy, hydro power, wind energy and sunlight are becoming more and more common. Renewable energy provided approximately 5.5% of the Netherlands energy production in 2014 and set to reach 14% in 2020 [1]. One of the main complications relying completely on renewable energy is the non consistency in the production. During the day wind velocity and solar intensity continuously change causing a short term fluctuation in the energy supply. Next to the daily fluctuations, monthly or even season wide fluctuations in renewable energy need to be compensated. for example wind energy, almost 50% of the energy is produced from November till February, while the remaining 50% is spread over the remaining eight months [2]. Those enormous fluctuations of several billions of kWh [2] must be stored in order to sustain a stable energy supply throughout the year. One of the most efficient ways to store energy is by storing the energy in batteries. The energy density, however is quite low, with approximately $30\,\mathrm{W\,h\,kg^{-1}}$ to $40\,\mathrm{W\,h\,kg^{-1}}$ it requires more than a trillion Kg of lead batteries to store the current fluctuation in wind energy. Seasonal energy storage in batteries is therefore simply not possible. Another energy storage solution is by storing the excess energy chemically for example by producing ammonia or hydrogen molecules. The produced molecules can easily be stored, have a high energy density and can be used to produce electricity when required. Splitting water in hydrogen and oxygen is a difficult process which requires highly active catalyst and currently platinum is the best viable option. Platinum, being a scarce and expensive metal, causes the prices of electrolyse cells to be high thereby reducing the cost efficiency of hydrogen production. In order to improve the cost efficiency new, abundant and cheap materials for hydrogen production need to be found. A promising new candidate is the photo-electrochemical tandem cell which is shown in figure 1.1. The tandem cell combines a photocathode at which hydrogen is evolved with a photoanode at which oxygen is evolved. Theoretical an external potential of $1.23\,\mathrm{V}$ is required to split water into H_2 and O_2. Both the photocathode and pho-

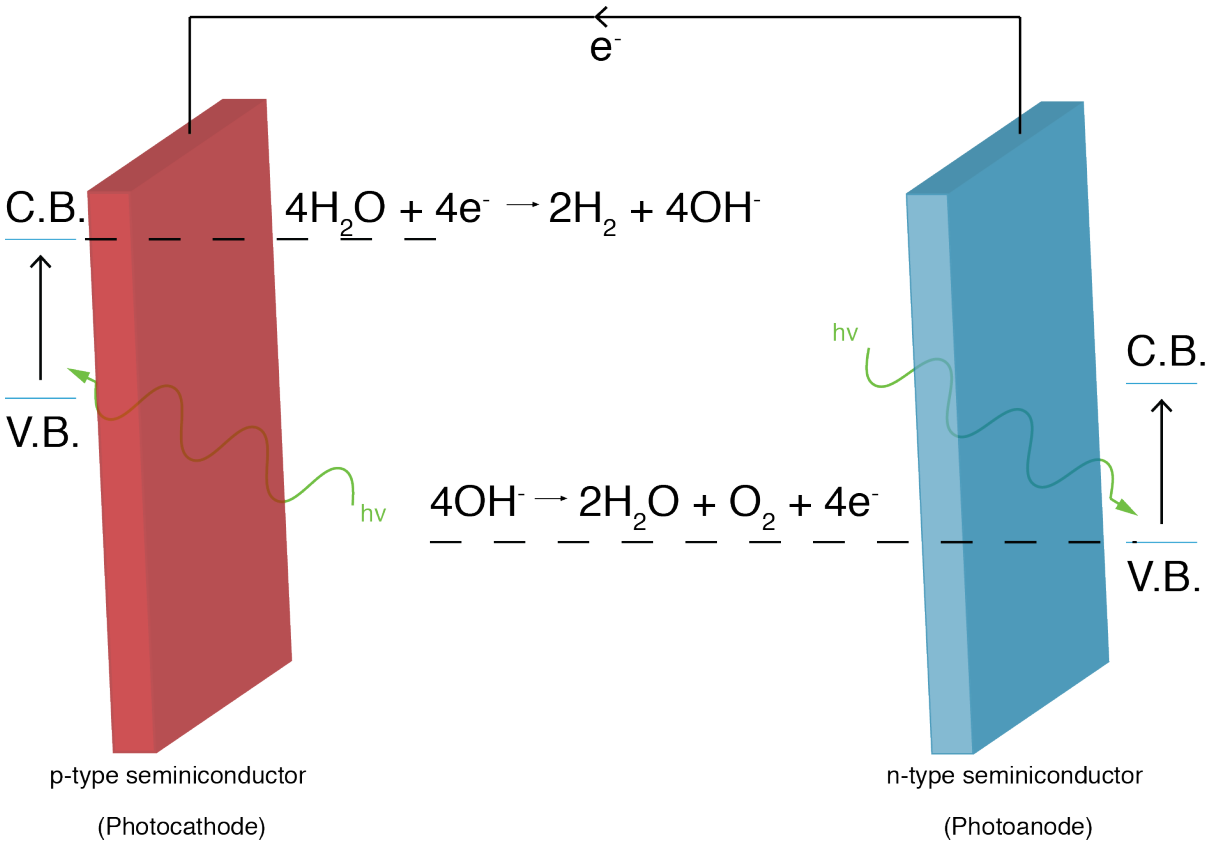

Figure 1.1: Schematical representation of the photoelectrochemical tandem cell.

toanode are semiconductor materials and create a potential when illuminated with solar radiation. Ideally this potential is enough to split water, however due to several losses a small external potential is required. In a tandem cell the hydrogen evolution reaction (HER) an the oxygen evolution reaction (OER) are placed in an electrolyte which should be conductive to close the electrical circuit. Furthermore the concentration of protons and hydroxide is important for the speed of the reaction and the stability of the materials. A high concentration of protons is beneficial for the HER however the photoanode is easily oxidized due to the negative voltage and a stable photanode is yet to be found. Finding a photocathode stable in basic media has shown to be difficult, however Sivula *et al* [3–6] demonstrated delafossite $CuFeO_2$ to be suitable for hydrogen evolution and proven stability in basic media.

Previous work showed that delafossite $CuFeO_2$ has correct band edges for hydrogen evolution [7, 8]. Recently different synthesis methods and activation treatments for delafossite $CuFeO_2$ were proposed [4–6, 9–18]. Currently, laboratory synthesis is often based on either chemical vapor deposition (CVD) or sol-gel based. However, both methods require long reaction times and both cannot be scaled to industrial sizes and can therefore not be commercially viable. In order to improve the scalability and reduce time while retaining the high quality of CVD thin films, ultrasonic spray pyrolysis (USP) is proposed. In ultrasonic spray pyrolysis (USP) the precursors are decomposed to a gaseous state similar to CVD and therefore a similar quality can be produced. Due to the facile working mechanism of the reaction setup, ultrasonic spray pyrolysis is highly scalable up to industrial scale.

The second step of the reaction requires a heat treatment in order to reduce the material to the required delafossite $CuFeO_2$. Previously a 6 h to 8 h treatment at 600 °C to 800 °C under argon atmosphere was performed. In order to further decrease the costs a new low-cost method needs to be found. Recently microwave heating has received much interest since it can significantly reduce reaction times of heat treatments [19]. A hybrid microwave annealing(HMA) method surpasses heat transfer limitations in conventional ovens by directly heating the sample. To further improve the results a microwave susceptor is frequently used [19]. A susceptor interacts strongly with the microwave radiation and will allow for shorter treatment times. In addition to the reduction in time it allows for more homogeneous heating by a two way heating system. Microwave radiation affects the core of the material while radiation from the hot susceptor affects the outer layers of the sample.

Post annealing treatments have been applied to further increase the performance. A 300 °C treatment results in oxygen intercalation and improves the performance upto 50% [4, 10].

Chapter 2

Theory

In this chapter the theory regarding spray pyrolysis, hybrid microwave annealing and numerous analysis techniques to confirm the structure, phase and performance will be explained.

2.1 Spray Pyrolysis

A precursor solution containing the required elements and a carrier gas are led to a atomizer in which the solution is atomized into small droplets. The droplets are carried to a heated substrate at which the solvent evaporates and the precursor decomposes hereby depositing the required atoms on the surface. A schematic presentation of the setup is shown in Figure 2.1.

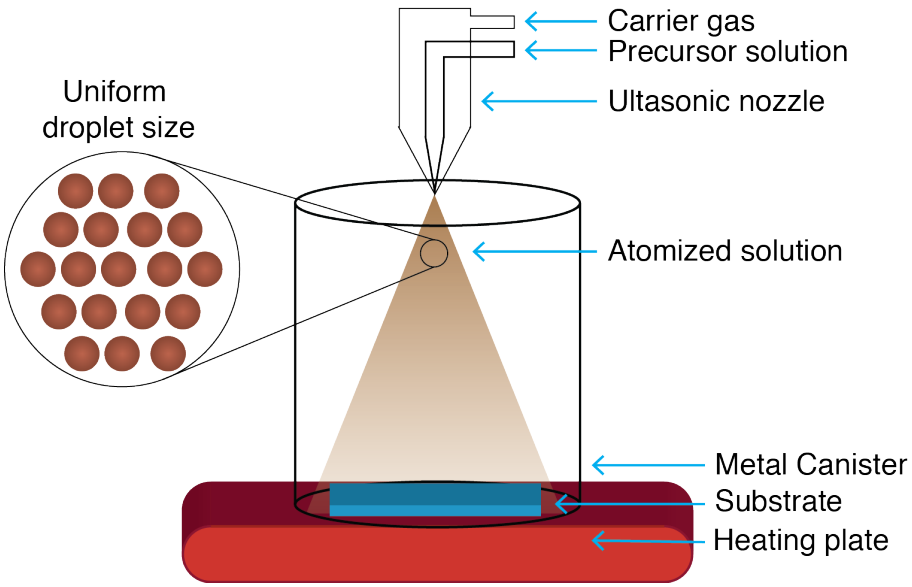

Figure 2.1: Schematic representation of the reaction setup including the atomizer, heating plate, substrate and enlargement of the droplets.

2.1.1 Atomisation

The first step in spray pyrolysis is atomizing the precursors solution to generate small droplets which can be send to the heated substrate. Mainly used nozzles use air blast, ultrasonic or electrostatic techniques to atomize the solution. The main differences are the rate of atomisation, droplet size, droplet size dispersion and the velocity of the droplets. A.J. Kelly has shown that the droplet size only depends on the charge density level ρe via the following relation. [20]

$$r^2 = \left(\frac{-a'}{\beta'}\right)\frac{3\epsilon_0}{q\rho_e} \tag{2.1}$$

where $\frac{-a'}{\beta'}$ is a constant value of $1.0x10^{-17}$J, ϵ_0 is the permittivity and q is the elemental charge. The droplet size and the initial velocity together determine the evaporation rate, the velocity at which it hits the substrate and the flight time of the droplet. The air blast

Table 2.1: Droplet diameter and velocity if frequently used atomizers for spray pyrolysis

Atomizer	Droplet diameter (μm)	Initial velocity (m/s)
Air blast	5 - 50	5 - 20
Ultrasonic	1 - 100	0.2 - 0.4
Electrostatic	5 - 70	1 - 4

nozzle are the most affordable however, the droplet size dispersion is high which results inhomogeneity in the films. Electrostatic nozzles give a good size dispersion however it is also the most expensive nozzle. Ultrasonic atomizers combine a good size dispersion and good controllability with acceptable costs and is often used.

2.1.2 Droplet Transport

After atomisation the droplets are transported to the substrate in the carrier gas. During the transport the solvent will evaporate and, depending on the substrate temperature, the precursor will decompose. Figure 2.2 shows four different pathways a droplet can have during the transport in which the droplets undergo chemical and physical changes. During the flight the gravitational, electrical, stoke and thermophoretic force act on the droplets thereby determining their trajectory and velocity. The impact of the forces changes along the pathway because of the changing size and weight of the droplets.

Gravitational Force

The gravitational force is only dependent of the mass of the droplet, which is calculated from the volume of the spherical particle times its density(ρ). Equation 2.2 gives the gravitational force, F_g, which is pulling the droplet to the substrate.

$$F_g = \frac{4\pi}{3}\rho r^3 g \tag{2.2}$$

With g the gravitational acceleration of 9.81 m/s^2

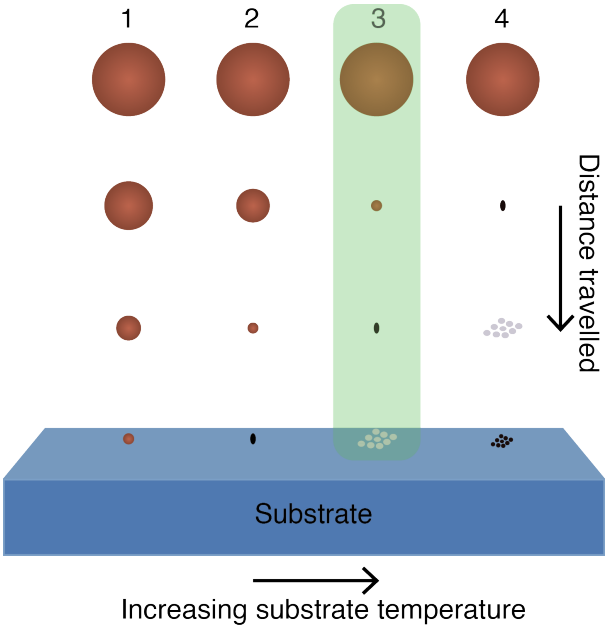

Figure 2.2: Change in aerosol droplets during transport from nozzle to substrate depending on the substrate temperature.

Electrical Force

In ultrasonic atomizers a plate is vibrated at ultrasonic frequencies using an electric generator. The generated force usually is orders of magnitude larger than the gravitational force and therefore the main force driving the droplets down to the substrate. The electric force is given by

$$F_e = q_d E \tag{2.3}$$

were q_d is the charge of the droplet and E is the generated electrical force. q_d is given by

$$q_d = q_{max} \frac{t}{t + t_0} \tag{2.4}$$

with

$$q_{max} = 8\pi\sqrt{\gamma \epsilon_0 r^3} \; and \; t_0 = \frac{4}{bdivE} \tag{2.5}$$

where ϵ_0 is the electrical permittivity, γ is the surface tension and b is the ionic mobility.

Stokes Force

The stokes force is caused by the friction between the droplet and air molecules and will slow the particles down. The force depends on the velocity and size of the particles and is given by

$$F_S = 6\pi\eta(v_d - V_a)\left(1 + \frac{3}{8}Re\right) \tag{2.6}$$

in which $(v_d - V_a)$ is the difference between the droplet and air velocity, η_a is the viscosity of air and Re is the Reynolds number which, for a spherical particle, is given by

$$Re = \frac{2r(Vd - Va)\rho_a}{\eta_a} \tag{2.7}$$

in which ρ_a is the air density.

Thermophoretic Force

The thermophoretic force is a force resulting from a temperature gradient caused by the heating plate. The first 10mm above the plate will have high temperature gradient causing the particles to slow down just above the substrate. The thermophoretic force is given by

$$F_t = \frac{3\pi\eta_a^2 r}{\rho_a} * \frac{\bigtriangledown(T_d)}{T_a} \tag{2.8}$$

where T_d and T_a are the droplet and air temperature respectively. $\bigtriangledown(T_d)$ is given by

$$\bigtriangledown(T_d) = \frac{3\kappa_a}{2\kappa_a^2 + \kappa_d} * \bigtriangledown(T_a) \tag{2.9}$$

With κ_d the thermal conductivity of the droplet and κ_a the thermal conductivity of air.

2.1.3 Precursor Solution Evaporation

Depending on the temperature of the plate and the four above mentioned forces, four different pathways for the droplet to reach the substrate arise. Figure 2.2 shows the illustrations of the four pathways (A to D)

Pathway A

In the first pathway a combination of a low temperature and large initial droplets leads to a low evaporation and therefore the droplets do not evaporate before reaching the substrate. On impact with the heated substrate, the droplet is evaporated and the precursor is decomposed. Both processes require heat and therefore the substrate temperature is lowered. Lowering the temperature impacts the reaction kinetics which alters the formation of the required oxide. This can be seen as spots in the final film and creates a rough surface.

Leidenfrost effect

When a droplet comes in contact with a materials at a temperature well above the boiling point of the solution a gaseous layer is formed between the droplet and the material. Due to the gaseous layer, the droplet will float on top of the surface and will either implode and cause damage to the surface or fall of the substrate leading to no deposition at all. This effect will play in important role in pathway A and will further reduce the quality of the thin film.

Pathway B

The higher temperature in the second pathway causes the droplets to fully evaporate before reaching the substrate. After evaporation of the solvent, the precursor is partially decomposed and a combination of salt and dry precipitate hits the substrate. The partial decomposition at the surface leads to hole formation in the film and thereby reducing the quality.

Pathway C

Further increasing the temperature causes the precursor to fully decompose during flight and forming a gaseous state just before impact. On impact the substrate vapor will undergo a heterogeneous reaction similar to chemical vapor deposition(CVD) and will result in the highest quality films.

Pathway D

Increasing the temperature even more causes the precursor vapor to form early and reacting before reaching the substrate. An oxide powder is formed before reaching the substrate and will not further react on impact with the substrate. This will lead to low deposition of the required oxide on the substrate.

2.1.4 Substrate

Substrates in tandem cells require conductivity to have a proper connection between the photocathode and photoanode. In multiple layer systems absorption of the top layers decreases the performance of the semiconductor significantly and back illumination is required. With back illumination, the light passes through the substrate before reaching the sample and therefore the substrate needs to be transparent for solar radiation. The combination of conductivity, transparency and a high band gap is rarely seen and most often a transparent conductive oxide (TCO) is chosen. The most frequently used TCO in industry is tin doped indium-oxide however, indium is rare and therefore an expensive material [21]. As mentioned before, the driving force behind delafossite copper iron oxide photocathodes, is the potential cost effectiveness of the material. In order to improve the cost efficiency a different TCO was chosen, fluorine doped tin oxide(FTO).

Fluorine Doped Tin Oxide

Tin oxide is a semiconductor material with a filled O^{2-} 2p valence band and an empty Sn^{4+} conduction band. With a bandgap 3.7 eV the tin oxide absorbs light with wavelengths below 350 nm. Delafosite $CuFeO_2$ in the tandem is designed to absorb near the infrared region and therefore SnO_2 has no negative effect on the performance of the thin film. As mentioned before, SnO_2 is a semiconductor material and therefore has a low conductivity. By doping tin oxide with fluorine, an electron rich ion, a N-type semiconductor

Table 2.2: Conductivities of different insulating, semi conducting and conducting materials used during hybrid microwave annealing [17, 22, 24]

Material	Conductivity $(\text{ohm m})^{-1}$
Quartz	10^{-17}
FTO	$1.67 * 10^2$
Glass	10^{-12}
$CuFeO_2$	0.67
Graphite	$3 * 10^4$

is created. The fluorine dopant leads to an increase in conductivity while remaining a similar bandgap and thereby a conductive transparent material is synthesized.

2.2 Hybrid Microwave Annealing

Microwaves are known as electromagnetic waves with a wavelength between 100 cm to 0.1 cm. The energy of microwave radiation is close to the bonding energy of atoms in molecules. Microwave radiation can interact with different bonds and thereby exciting to molecule to a higher energy state. Depending on the material, the interactions can be both electric and magnetic. The electric interaction mainly depends on the dielectric constant(ϵ'), which determines the ability to store electric energy, and the dielectric loss(ϵ''), which determines the ability to convert the stored electric energy into heat. The magnetic interaction depends on two comparable properties, the permeability(μ') and the magnetic loss(μ''), which are the ability to store and convert magnetic energy to heat respectively. The electric energy can be stored by polarizing dipole bonds, for example O-H bonds. The conversion of the stored energy occurs via relaxation(polarization loss) and via conduction of free electrons (conduction loss). The effective dielectric properties, considering dipolar, interfacial, ionic and electronic polarization mechanisms, can be written as [22, 23]

$$\epsilon' = \epsilon'_{dipolar} + \epsilon' interfacial + \epsilon' ionic + \epsilon' electronic, \tag{2.10}$$

and

$$\epsilon'' = \epsilon'' dipolar + \epsilon'' interfacial + \epsilon'' ionic + \epsilon'' electronic + \frac{\sigma}{2\pi f} \tag{2.11}$$

Were σ is the conductivity of the material and f is the microwave frequency which can be calculated using the wavelength (λ) and the phase velocity (ν).

$$f = \frac{\nu}{\lambda} \tag{2.12}$$

Table 2.2 shows the conductivities of the different materials used in the hybrid microwave treatment. In highly conductive materials, such as graphite, the conduction loss is the primary contribution for heating. In less conductive materials, for example glass or quartz, the conduction loss is close to zero and the polarization loss is the main contributor for heating. Walkiewicz *et al* [25] showed heating rates of different materials in a commercial sharp 1000 W 2.45 GHz microwave. Heating rates up to 1283 °C min^{-1} were achieved

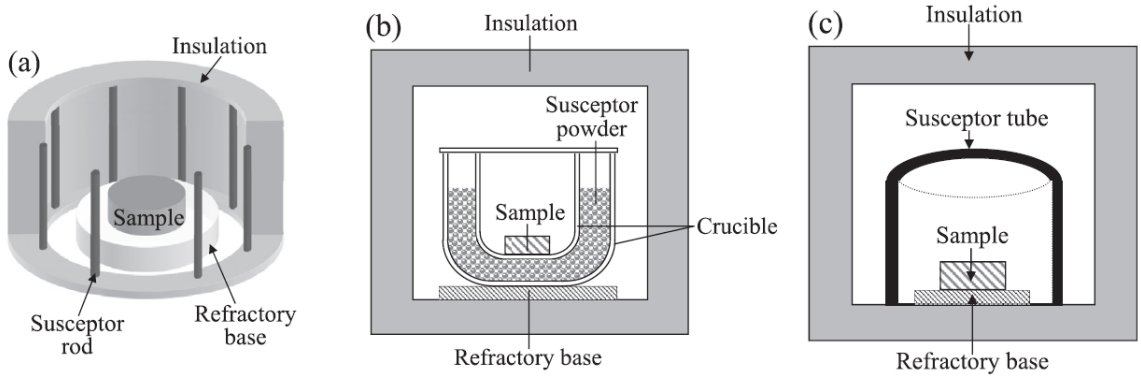

Figure 2.3: Schematic representation of the three main cell designs used in hybrid microwave annealing. With (a) rod-like, (b) powder and (c) tubular cell design. Reproduced from Bhattacharya *et al* [19]. susceptors.

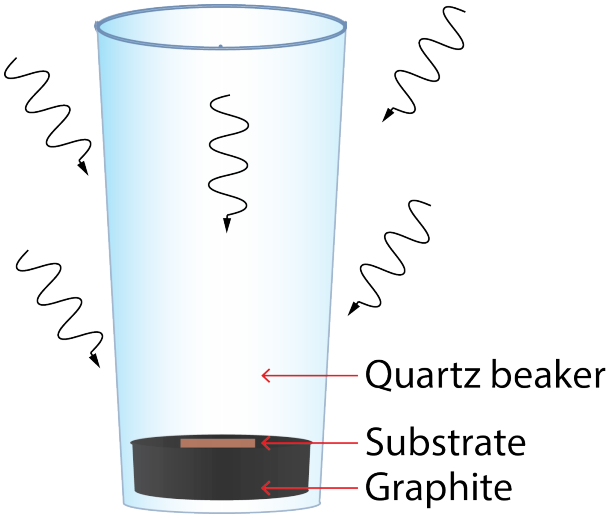

Figure 2.4: Final cell design used during hybrid microwave annealing

for highly conductive materials such as carbon powder and graphite. Non conducting materials however, showed long warm up times before reaching a critical temperature at which the dielectric loss undergoes a rapid change. Above the critical temperature the material changes from a near microwave transparent material to a strong interacting material.

Strong interacting materials continuously heat up to temperatures well above 1500 °C at which most products will be destroyed. In order to gain more control over the ramp and final temperature a microwave susceptor is used. The microwave susceptor is required to absorb the radiaton more easily than the sample itself. As a result the uncontrolled heating will occur in the susceptor instead of in the product. An additional effect of the use of a susceptor is the significant reduction in warm-up time for microwave transparent materials since the susceptor is able to transfer heat to material.

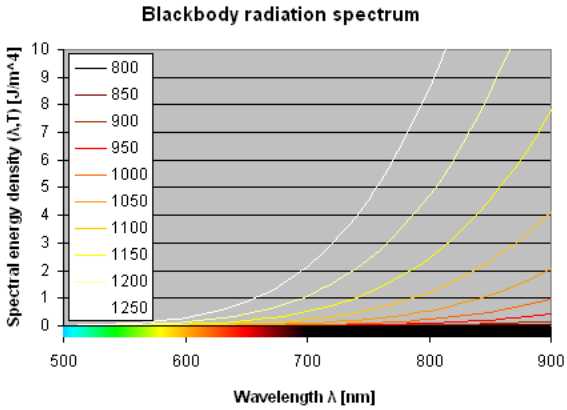

Figure 2.5: Backbody radiation in the visible spectrum at 800, 850, 900, 950, 1000, 1050, 1100, 1150, 1200 and 1250 K reproduced from [26]

2.2.1 Cell Design

In order to improve the reproduce-ability, different microwave cells were designed. All cells contain three major components, a microwave susceptor, an insulating chamber and a base for sample placement. Based on the previously reported cell designs shown in figure 2.3 a new cell was designed and is shows in figure 2.4.

2.2.2 Oxidation of Graphite

During the hybrid microwave annealing the temperatures of graphite can be estimated using the thermal radiation. In most cases the thermal radiation follows the ideal black body radiation trend thorougly described in the literature. Above the Draper point, approximately 525 °C, thermal radiation will become visible and all solids show a dim red color. With increasing temperature the color shifts to brighter yellow and eventually a bright white color. Using Plank's equation in the spectral radiance of an objects at a certain temperature can be calculated.

$$B = \frac{2hc^2}{\lambda^5} \frac{1}{e^{\frac{hc}{\lambda K_B T}} - 1} \tag{2.13}$$

In which h is Plank's constant, c is the speed of light and K_B is the Boltzmann constant. At hight temperatures the spectrum will be dominated by UV-radiation. However, when zoomed into the visible region the spectrum shown in figure 2.5 is acquired. Table 2.3 shows an overview of the different colors as observed by the human eye

By combining the subjective color indication[26] with previous results in hybrid microwave annealing [19] the temperature of graphite can be estimated from 1000 °C to 1400 °C. Above 500 °C graphite will slowly be oxidized by air and form carbon monoxide and carbon dioxide via the following reactions $C + \frac{1}{2} O_2 \longrightarrow CO$ and $C + O_2 \longrightarrow CO_2$ [27]. Since the graphite is in a closed system and heated to temperatures well above 500 °C oxygen is being depleted by the oxidation of graphite and a reducing atmosphere will arise.

Table 2.3: Color of a black body thermal radiator at different temperatures as seen by the human eye calculated using Planks equation.

480 °C	Faint red glow
580 °C	Dark red
730 °C	Bright red
930 °C	Bright orange
1100 °C	Pale Yellow
1300 °C	Bright Yellow
>1400 °C	White

2.3 Analysis Methods

2.3.1 Optical Spectroscopy

Optical spectroscopy is an important tool in semiconductor analysis. Using the Beer-Lambert law, the absorption and transmission can be calculated at different wavelengths.

$$\frac{I_1}{I_0} = 10^{-\epsilon c d} \tag{2.14}$$

in which I_0 and I_1 are intensity received by and transmitted by the the material respectively. ϵ is the extinction coefficient and d is the distance travelled trough the sample in centimetres.

Bandgap in semiconductors

Koffyberg *et al* [7] determined that the valence band of delafossite $CuFeO_2$ is mainly dominated by the 3d-band of copper and lies 4.9 eV below the vacuum level. At a deeper 7.1 eV lies the oxygen-2p band and the conduction band of delafossite $CuFeO_2$ lies at 3.7 eV. The bandgap for delafossite $CuFeO_2$ is indirect allowed and is approximately 1.4 eV. Direct allowed transitions occur at approximately 3.0 eV.

Tauc plot

In order to determine the direct and indirect band gap of delafossite $CuFeO_2$ the energy $(h\nu)$ can be plotted versus

$$(ah\nu)^{\frac{1}{r}}, \tag{2.15}$$

in which r changes for different transitions:

- r = 1/2 for direct allowed transitions
- r = 3/2 for direct forbidden transitions
- r = 2 for indirect allowed transitions
- r = 3 for indirect forbidden transitions

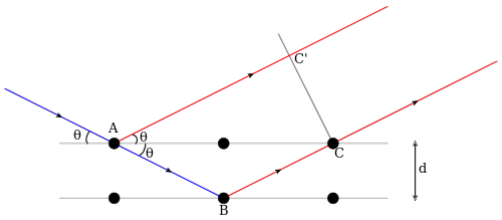

Figure 2.6: Schematic representation of the diffraction of the incoming beam (blue) into two constructively interfering outgoing beams at a certain lattice spacing (d) and angle θ

The resulting plot has a linear area which, if extrapolated to y = 0, shows the onset of the absorption band [28].

2.3.2 Thermogravimetric Analysis

Over time the mass of a sample is measured while the temperature increases. At certain temperatures the sample partially decomposes and forms gaseous products. Gas escapes the TGA chamber leading to a reduction in weight which is recorded by the balance. Often multiple regions appear in the weight loss diagram showing multiple water loss and decomposition steps.

2.3.3 X-Ray Diffraction

XRD is an analysis technique based on the constructive interference of diffracted x-ray radiation. The radiation of a specific wavelength(λ) is scattered at different angles depending on the lattice spacing (d) an follows Bragg's law:

$$n\lambda = 2dsin(\theta), \tag{2.16}$$

in which θ is the angle at which the constructive interference occurs. Figure 2.6 gives a schematic representation of the x-ray diffraction.

The delafossite crystal structure with space group R3m has a molecular structure of ABO_2 in which A and B are metal cations with a I and III plus charge respectively. In figure 2.7 a graphical representation of the crystal lattice is shown together with the corresponding x-ray diffraction pattern.

The shown XRD pattern is made using delafossite in a powder form which are different than thin film samples. The main difference is the random order in powders versus the growth of some preferential plane orientations in the thin films. During growth of the thin films some orientations will grow preferentially quicker than other orientations resulting in a different intensity ratio. Some peaks will be more pronounced while others will not be visible.

Next to delafossite other phases of copper and iron oxide are distinguishable with XRD the most import ones being cuprospinel ($CuFe_2O_4$, cupric oxide CuO and hematite Fe_2O_3.

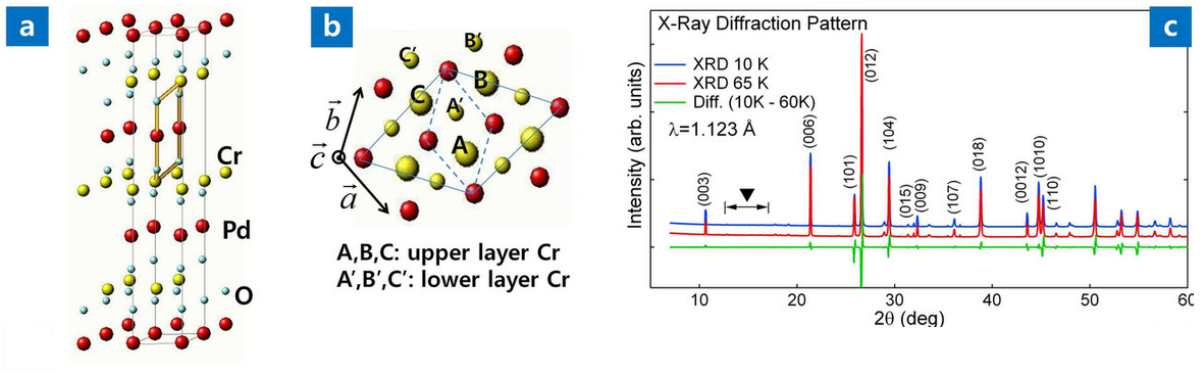

Figure 2.7: Delafossite crystal structure with corresponding x-ray difraction patterns reproduced from Noh *et al* [29].

2.3.4 Scanning Electron Microscopy

Electron microscopy is an analysis technique in which electron waves are used to analyse the interactions between waves and matter. Matter interacts with waves similar in size as the wavelength which in term determines the resolution of the spectroscopy method. The electron wavelength, called the Broglie wavelength, can be calculated using the momentum (p). The momentum is related to the mass (m) of an electron ($9.1 * 10^{-31}$) and the kinetic energy (T) via the following relation:

$$p = (2mT)^{1/2}, \tag{2.17}$$

the Broglie wavelength is then calculated using the following relation

$$\lambda = h/p, \tag{2.18}$$

in which h is Plank's constant ($6.625 * 10^{-34}$). In electron microscopy the energy of an electron therefore determines the resolution achieved. Electrons are accelerated using an electric field ranging from 10 kV to 50 kV which results in Broglie wavelengths in the order of pico meters. Due the short wavelength interactions with single atoms become visible and near atomic resolution is achieved.

When the high energy electron hits the surface of a material some of its energy is lost via various mechanisms. The lost energy can be converted to heat, light emission, low-energy secondary electrons or high-energy backscattered electrons. In conventional scanning electron microscopy (SEM) the signals from low-energy backscattered electrons are used to create a 2D image of the surface of a material. Since SEM is a surface technique thick samples can be analysed which simplifies sample preparation. The large samples are placed on a stage which can moved and rotated in all directions making it possible to analyse the complete surface of the material.

2.3.5 Energy Dispersive X-Ray Spectroscopy

In electron microscopy inelastic scattering of the electrons results in the excitation of atoms. The energetic electrons excite atoms to high energy levels and emit x-ray radiation when relaxation to the ground state occurs. Energy levels are specific for each atom and therefore the energy of the x-ray radiation is specific for an atom. By accurately analysing the x-ray radiation an element composition map can be constructed.

2.3.6 X-ray absorption spectroscopy

X-ray absorption(XAS) is used to determine the local chemical properties and gives information on the electronic and geometric structure. High energy photons, produced by a synchrotron, can excite core electrons with a binding energy ranging from 0.1 keV to 100 keV. The edges named according to the principal quantum numbers n=1, 2 and 3 which correspond to the K-, L- and M- edges. X-ray absorption(XAS) probes the empty valence state and will give information about the oxidation state of the atom.

2.3.7 Hard X-Ray Photoelectron Spectroscopy

XPS is a technique in which the surface chemistry of a sample is analyzed. Using an x-ray source, surface atoms are excited and the emission of various kinetic electrons is measured. A photoelectron spectrum is measured by counting electrons over a wide range of electron kinetic energies. The kinetic energy of the ejected electrons depends on the x-ray energy ($h\nu$) and the binding energy of the electron via the following relation:

$$E_k = h\nu - E_b, \tag{2.19}$$

in which E_b is the binding energy which depends on the element, the orbital and the chemical environment from which the electron was emitted. The photoelectron spectrum therefore contains information about the elemental composition, emperical formula and oxidation state of the elements within the top 5 nm to 10 nm of the material. Different excitation energies can be used to probe either surface atoms 0.5 nm to 1 nm or bulk atoms up to several nanometer.

2.4 Photoelectrochemical Tests

In order examine the electrochemical properties of the materials, various measurements were performed on the samples. Measurements are performed in an Teflon photoelectrochemical cell which contains:

- Reference electrode, used to measure the potential of the working electrode
- Counter electrode, used to pass current through the working electrode
- Working electrode, which is the sample on which the measurements are performed
- Electrolyte, to allow conductivity between electrodes
- Window, to allow illumination with solar radiation

2.4.1 Cyclic Voltametry

In cyclic voltametry(CV) the potential is ramped between an upper and lower potential and the current produced by the working electrode is plotted versus the set potential. CV measurements can be used to find the following properties:

- The onset potential, the potential on which the sample starts converting light into electricity
- The photocurrent, the current produced by the sample when illuminated by solar radiation
- Stability, a different result every cycle indicates an unstable sample

CV gives a good indication of the properties of the material and based on those properties follow-up measurements can be performed.

2.4.2 Chronoamperometry

The potential is set to a constant value and the current produced by the working electrode is measured over time. Using a beam chopper to create chopped light both the dark and light current can be recorded simultaneously. Chronoamperometry(CA) is performed for longer times to gain better insight in the performance and stability of the working electrode.

2.4.3 Incident Photon-to-Current Efficiency

To gain more insight in the efficiency of the material an incident photon to current efficiency(IPCE) measurement is performed. The rate of the photocurrent, generated by the working electrode, is divided by the incident photon rate at different wavelengths. As a result the quantum efficiency(QE) is calculated for each wavelength and can be used to calculate the bandgap of the material.

Chapter 3

Experimental Methods

3.1 Chemicals

Table 3.1: List of chemicals with purity and source used during research.

Name	Purity	Source
DMF	99.8	Fisher
Ethanol	99.8	Acros
$Cu(NO_3)_2 \cdot 3\,H_2O$	99	Acros
$CuCl_2$	99.99	Aldrich
$Cu(C_5H_7O_2)_2$	99	Alfa Aesar
$Cu(C_2H_3O_2)_2$	99.99	Aldrich
$FeCl_3$	97	Sigma Aldrich
$FeC_5H_7O_2)_3$	99	Acros
HCl	37	Emsure
NaOH	99	Emsure
H_2O_2	50	Sigma Aldrich
NaH_2PO_4	99	Sigma Aldrich
Na_2HPO_4	99	Sigma Aldrich

3.2 Substrate Preparation

Commercial FTO coated glass was cut into 3 x 1.5 cm fragments. Both sides were mechanically cleaned with CIF twice and placed in a mixture of ethanol, acetone and water. The fragments were placed in ultrasound bath, 45 kHz and 100 W, for 15 min. Afterwards the solution was changed for 1 M HCl followed by another 15 min ultrasound. The fragments were rinsed with demi water after each step and were stored in $d-H_2O$. Before the reaction the fragments were dried with N_2 and placed in UV/Ozone procleaner (Bioforce) for 15 minutes.

3.3 Spray pyrolysis

In a typical experiment, $Fe(C_5H_7O_2)_3$ (FeAcAc) (80mM) and $Cu(NO_3)_2 \cdot 3H_2O$ (34mM) were dissolved in DMF and stirred overnight. The resulting solution was deposited using ultrasonic-spray pyrolysis on cleaned FTO substrate at 450 °C. For the atomisation of the solution a Sonaer 60 kHz nozzle narrow spray equipped with a wide vortex was employed, fixing the power from 1.8 W to 2.2 W. The precursor solution was dispensed through a single micro-feed channel with a flow rate of $2\,mL\,min^{-1}$, and compressed N_2 with a flux of $2\,L\,min^{-1}$ was employed as carrier gas. One spray pyrolysis cycle consisted of

- 20 s spray pyrolysis
- 15 s reheating
- 20 s spray pyrolysis
- 15 s reheating

, providing an average of 10 nm film growth per spray pyrolysis cycle. After deposition, the films were slowly cooled to room temperature to prevent the substrate from cracking due to heat shock.

3.3.1 Investigated Parameters

- Cu and Fe precursors
- Solvent
- Concentration
- Liquid flow
- Carrier Gas
- Gas flow
- Deposition temperature
- Precursor temperature

3.4 Heat Treatment

In order to improve the homogeneity and crystallinity of the thin films, a heat treatment was performed. The samples were placed in a muffle oven and heated to 550 °C in 3 h and kept at that temperature for 3 h. Afterwards the thin films are cooled to room temperature overnight.

3.4.1 Investigated Parameters

- Heating ramp

- Annealing temperatures
- Annealing time
- Cooling ramp

3.5 Hybrid Microwave Annealing

After deposition, the films were placed in a quartz beaker filled with 8 g of graphite powder. The graphite was partially compressed in the central area were the sample was placed and uncompressed near the border of the setup, see figure 2.4. The quartz beaker was closed using a ceramic lid and placed in a commercial microwave (Sharp 2.4 GHz 800 W) and microwaved for 4 min to 7 min.

3.5.1 Investigated Parameters

- Type of graphite
- Amount of graphite
- Compression of graphite
- Sample placement
- Quartz beaker location
- Microwave duration

3.6 Analysis

The electronic transitions and bandgap were studied using UV-VIS-NIR spectrometer. Both transmission and absorption spectra were recorded from 900 nm to 350 nm. Using a D2 (Bruker) diffractometer, equipped with a Co Kα X-Ray source excited at 30 kV and 10 mA, the X-ray diffraction patterns were acquired from 20° to 80° 2θ angles. The acquisition conditions for the diffractograms were 0.04° step size and 2 s integration time. Scanning electron microscopy(SEM), using of a FEI Helios Nanolab 600 FIB-SEM instrument at 5 kV acceleration voltage, was used to acquire detailed information of the surface and thickness of the material. Photo electrochemical measurements were performed using an autolab potentiostat, Pt reference electrode and Ag/AgCl counter electrode all in a 200 mM solution of NaOH. The PEC cell was illuminated using a Hamamatsu 75 W Xenon arc lamp fitted with a 1.5 AM filter and callibrated to 100 mW cm^{-2}. A commercial beam chopper was used to chop the beam with a four second interval.

Chapter 4

Spray pyrolysis

In order to find the most suitable precursors, solvent and reaction temperature various combinations viable combinations were tested and shown in table 4.1.

4.1 Solvent Influence

As explained in the theory, the solvent has a major effect in spray pyrolysis and the most important parameters are the polarity, for the solubility of the precursors, and the surface tension for the atomisation. Since all precursors are inorganic salts a polar solvent is required. Water being the most obvious polar solvent has the highest solubility for all the precursor salts. Unfortunately using water as the solvent resulted in rough non conformal films as can be seen in figure 4.1. Low concentrations of precursor were used in order to exclude the influence of the concentration on the roughness. Additionally the temperature was increased to shift to pathway C in figure 2.2. Unfortunately all films remained rough and non conformal it may be caused by accumulation of droplets leading to a large size dispersion. A large dispersion causes the deposition rate to change constantly throughout the reaction. As a result rough and non conformal films arise which makes them unsuitable for further treatment and therefore another solvent was required.

Ethanol is less polar than water and therefore has a lower solubility for the precursor salts. Fortunately in spray pyrolysis the concentrations are ranging from 1 mM to 100 mM and all salts could be dissolved in the required concentrations. Thin films prepared using ethanol showed no visible roughness, however the films were very thin as can be seen in figure 4.1. It could be explained by quick evaporation of the solvent because of the low boiling point of ethanol. In order to increase the thickness the temperature was lowered however this resulted in lower quality films. The lower temperature was approaching the decomposition temperature of the various precursors as described in the literature. In order to confirm various TGA measurements were performed, figure 4.2 shows the decomposition of $CuCl_2$. Up to 100 °C a 20% reduction in weight is observed which is ascribed to the evaporation of water. A second reduction in weight occurs from 300 °C beyond 450 °C which is ascribed to the decomposition of $CuCl_2$. Figures B.3, B.1, 4.2, B.2 and B.4 show the thermogravimetric analyses of the remaining precursors. Decomposition temperatures up to 375 °C were found and therefore a higher deposition temperature is

Table 4.1: Different combinations of solvents, precursors en temperature used with spray pyrolysis to determine the ideal conditions

Solvent	Iron precursor	temperature	Copper precursor
DMF	$Fe(AcAc)_3$	350 °C	$Cu(NO_3)_2$
DMF	$Fe(AcAc)_3$	350 °C	$Cu(C_2H_3O_2^-)_2$
DMF	$Fe(AcAc)_3$	350 °C	$Cu(AcAc)_2$
DMF	$Fe(AcAc)_3$	350 °C	$CuCl_2$
DMF	$Fe(AcAc)_3$	400 °C	$Cu(NO_3)_2$
DMF	$Fe(AcAc)_3$	400 °C	$Cu(C_2H_3O_2^-)_2$
DMF	$Fe(AcAc)_3$	400 °C	$Cu(AcAc)_2$
DMF	$Fe(AcAc)_3$	400 °C	$CuCl_2$
DMF	$Fe(AcAc)_3$	450 °C	$Cu(NO_3)_2$
DMF	$Fe(AcAc)_3$	450 °C	$Cu(C_2H_3O_2^-)_2$
DMF	$Fe(AcAc)_3$	450 °C	$Cu(AcAc)_2$
DMF	$Fe(AcAc)_3$	450 °C	$CuCl_2$
Water	$Fe(AcAc)_3$	350 °C	$Cu(NO_3)_2$
Water	$Fe(AcAc)_3$	350 °C	$Cu(C_2H_3O_2^-)_2$
Water	$Fe(AcAc)_3$	350 °C	$Cu(AcAc)_2$
Water	$Fe(AcAc)_3$	350 °C	$CuCl_2$
Water	$FeCl_3$	350 °C	$Cu(NO_3)_2$
Water	$FeCl_3$	350 °C	$Cu(C_2H_3O_2^-)_2$
Water	$FeCl_3$	350 °C	$Cu(AcAc)_2$
Water	$FeCl_3$	350 °C	$CuCl_2$
Ethanol	$FeCl_3$	350 °C	$Cu(NO_3)_2$
Ethanol	$FeCl_3$	350 °C	$Cu(C_2H_3O_2^-)_2$
Ethanol	$FeCl_3$	350 °C	$Cu(AcAc)_2$
Ethanol	$FeCl_3$	350 °C	$CuCl_2$
Ethanol	$FeCl_3$	400 °C	$Cu(NO_3)_2$
Ethanol	$FeCl_3$	400 °C	$Cu(C_2H_3O_2^-)_2$
Ethanol	$FeCl_3$	400 °C	$Cu(AcAc)_2$
Ethanol	$FeCl_3$	400 °C	$CuCl_2$
Ethanol	$Fe(AcAc)_3$	350 °C	$Cu(NO_3)_2$
Ethanol	$Fe(AcAc)_3$	350 °C	$Cu(C_2H_3O_2^-)_2$
Ethanol	$Fe(AcAc)_3$	350 °C	$Cu(AcAc)_2$
Ethanol	$Fe(AcAc)_3$	350 °C	$CuCl_2$
Ethanol	$Fe(AcAc)_3$	400 °C	$Cu(NO_3)_2$
Ethanol	$Fe(AcAc)_3$	400 °C	$Cu(C_2H_3O_2^-)_2$
Ethanol	$Fe(AcAc)_3$	400 °C	$Cu(AcAc)_2$
Ethanol	$Fe(AcAc)_3$	400 °C	$CuCl_2$

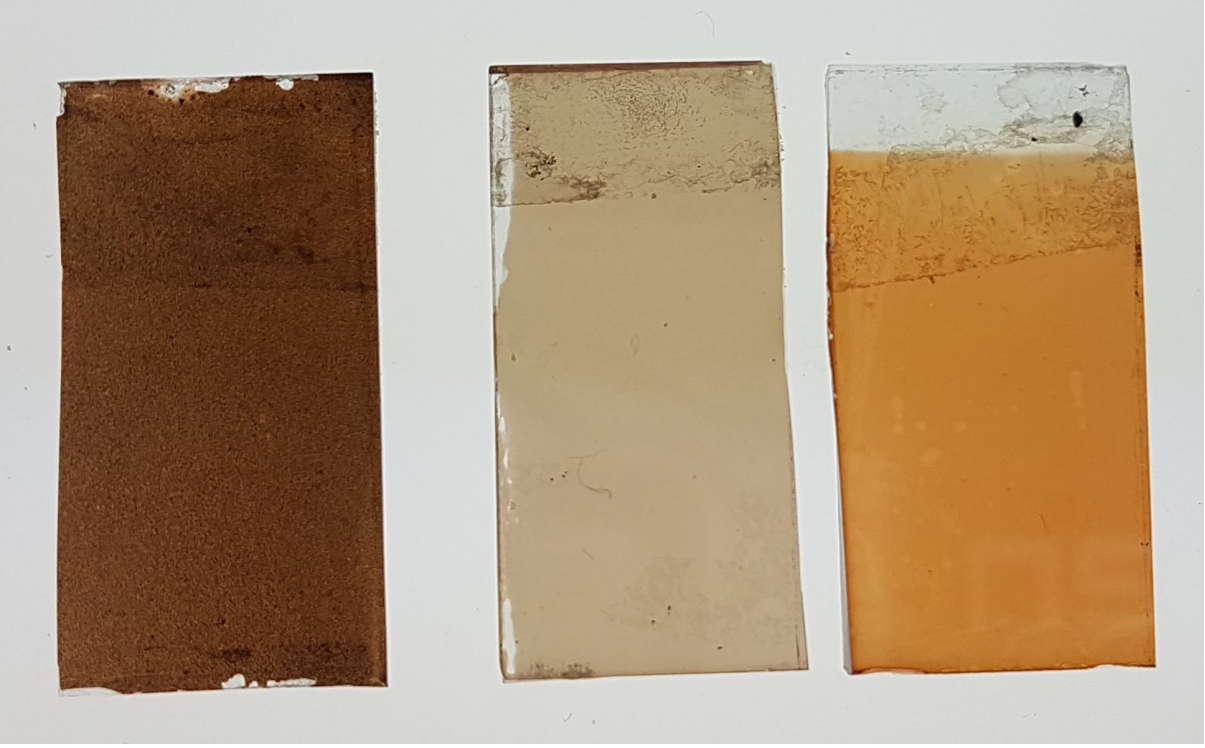

Figure 4.1: Optical image of copper iron thin films made using, from left to right, water, ethanol and DMF as solvents for the precursor solution. A rough surface can be observed in the thin film made using water and it can be seen than DMF results in a thicker, more opaque thin film.

required. A higher decomposition temperature increases the evaporation rate and changes both the deposition pathway and rate. In order to reduce solvent evaporation and improve the deposition of both copper and iron a higher boiling solvent was required.

Frequently used polar high boiling solvent is dimethylformamide (DMF) which has a boiling point of 153 °C. Most precursor salts were soluble in DMF except $FeCl_3$ all other precursor combinations were tested at various temperatures and immediately a faster deposition was noticed and thicker films were formed. The temperature 450 °C resulted in the most optically reflecting films which indicates a flat surface. The quality of films prepared with ethanol or DMF is comparable however, the deposition rate is highest when using DMF and was therefore preferred. During the following reactions both ethanol and DMF are used to further determine the best reaction conditions.

4.2 Precursor Determination

$FeCl_3$ in combination with either $CuCl_2$ or $Cu(NO_3)_2$ gave low quality films while the quality improved when used in combination with copper acetate or copper acetylacetonate (acac). On the contrary combining iron acac with either $CuCl_2$ or $Cu(NO_3)_2$ resulted in high quality films while combining with iron acac with copper acac gave low quality films. It is therefore believed that having some organic precursor leads to higher quality films however excess carbon will reduce the quality. In order to confirm the result acetylacetone was added to a mixture of iron chloride and copper nitrate in ethanol. The resulting films

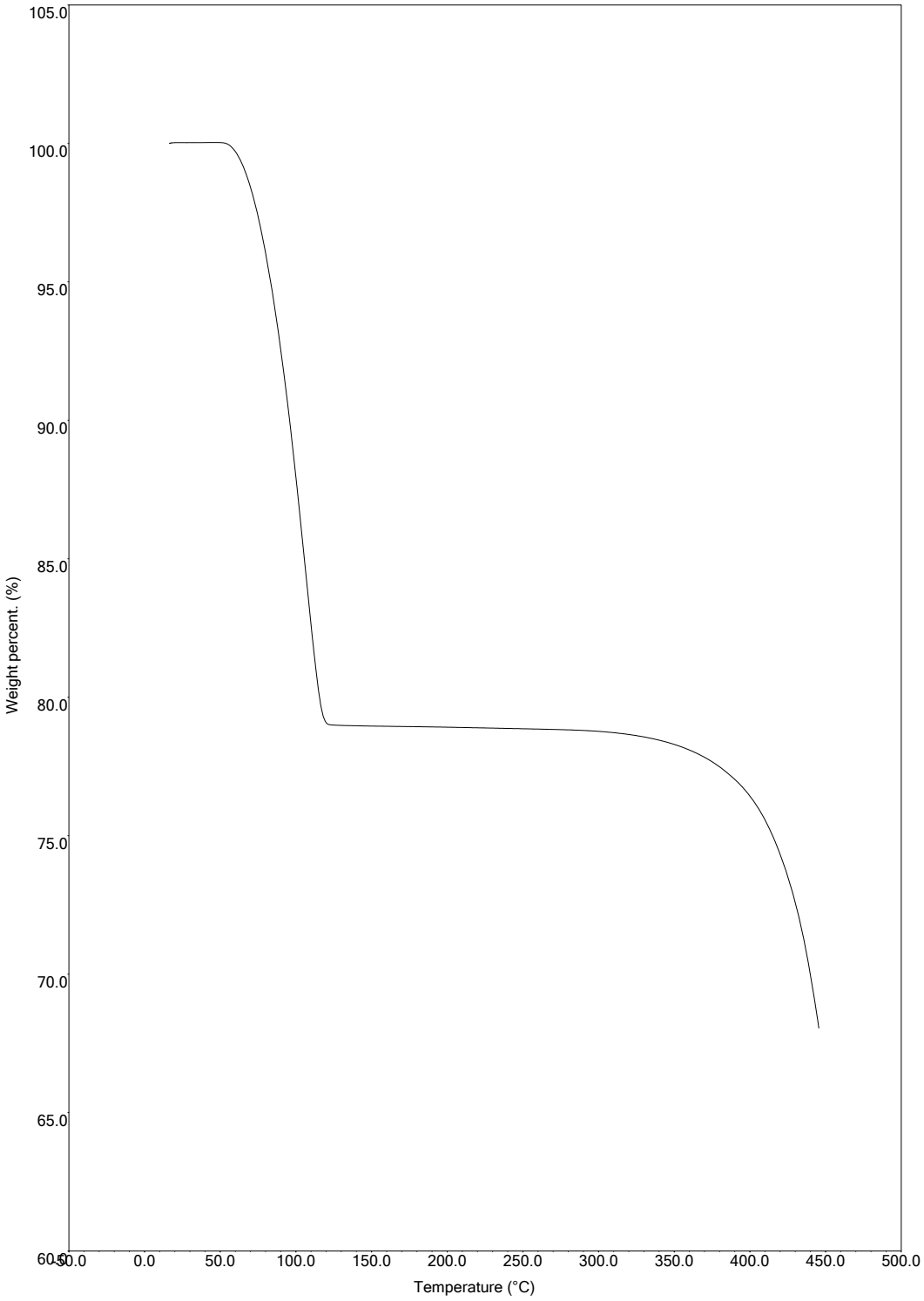

Figure 4.2: Thermogravic analysis of $CuCl_2$ from 20 °C to 450 °C with a ramp of 10 °C s^{-1}.

where of high quality and thereby the requirement of an organic precursor was confirmed. Different concentrations of acac were tested and a ratio of iron to acac of 1 to 3 resulted in the highest quality films. $Fe(AcAc)_3$ intrinsically has the 1 to 3 ratio and was therefore chosen as ideal iron precursor. Combination with either copper chloride or nitrate lead to highest quality films. The decomposition temperature of $CuCl_2$ is reaching the optimal deposition temperature of 450 °C and was not completely decomposed on impact. As a result residual chlorine species were incorporated in the photocathode thin films. Removal of those species required high temperature treatments well above 550 °C. Copper nitrate decomposed at lower temperatures and does not require any high temperature treatment to remove residual species and was therefore chosen as most promising precursor/.

4.3 Stoichiometric Copper Iron

4.3.1 Scanning Electron Microscopy - Energy Dispersive X-ray Spectroscopy

The stability of the thin films mainly depends of the presence of other phases present in the film. A stoichiometric amount of copper and iron is required to synthesise delafossite $CuFeO_2$. Deposition rates of copper and iron differ and therefore an ideal precursor ratio needs to be determined. The concentration of iron acac was set to 20 mM while the concentration of copper nitrate was varied from 1 mM to 30 mM and the resulting films were analyzed with SEM-EDX.

An excess of copper leads to unstable CuO and excess iron leads to either cuprospinel $CuFe_2O_4$ or hematite Fe_2O_3. Both iron phases are stable during the PEC test however do not provide any positive effect to the photocurrent. The copper oxide phase however, is unstable during PEC test and will lead to degradation of the sample. In order to improve the stability a slight excess of iron was accepted for further optimization and therefore a copper nitrate concentration of 3.5 mM was chosen.

4.3.2 Inductively Coupled Plasma - Optical Emission Spectroscopy

After doing various XRD experiments no pure delafossite $CuFeO_2$ was found. A cuprospinel $CuFe_2O_4$ phase was often present and a pure iron phase hematite Fe_2O_3 was observed both indicating an excess of iron therefore ICP-OES measurements were performed to confirm the confirm the copper iron ratio. Three samples were prepared with 20 mM of iron and copper nitrate ranging from 3.5 mM to 5.5 mM and measured with SEM-EDX. After determining the ratio, the thin films were dissolved in aqua regia and the copper iron ratio was determined using ICP-OES both results can be found in table 4.2.

It can clearly be seen the SEM-EDX gives a three fold higher Cu/Fe ratio as the ICP-OES. It is believed copper atoms absorb emission from iron atoms during the SEM-EDX measurements leading to a lower iron signal. The ICP-OES gives a more accurate result and shows an excess of iron thereby explaining the presence of the cuprospinel $CuFe_2O_4$ and hematite Fe_2O_3 phases. From the results it was extrapolated that approximately 20 mM iron to 8.5 mM copper should result in a near stoichiometric ratio. A new batch

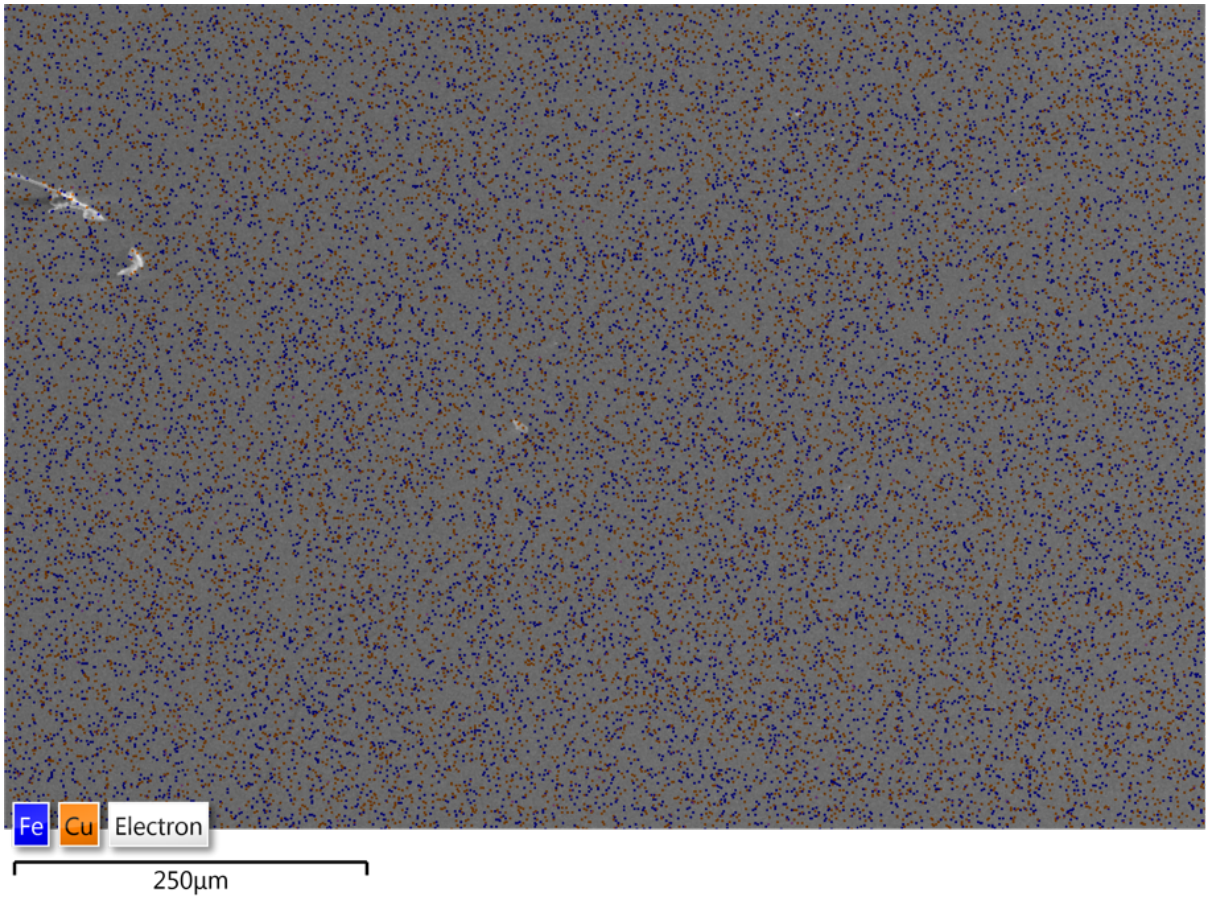

Figure 4.3: SEM-EDX map of a copper iron oxide thin film showing a homogeneous distribution of both copper(orange) and iron(blue) throughout the sample.

Table 4.2: Comparison between the copper to iron ratio in the precursor solution, the EDX result and in the ICP result.

Used ratio Fe - Cu	EDX result Cu/Fe	ICP result Cu/Fe
20 - 3.5	1.0	0.35
20 - 4.5	1.3	0.42
20 - 5.5	1.6	0.56

of samples with a higher copper concentration was produced using USP and were tested briefly using XRD in order to have an indication of the presence of other phases. In the 20 to 8.5 ratio no other phases where found while in other ratios either excess copper or excess iron phases were found. It was therefore chosen to continue with the ratio of 20 mM iron and 8.5 mM copper for further reactions.

Chapter 5

Post Reaction Treatments

After stoichiometric films were synthesized using spray pyrolysis an XRD diagram was measured which showed a mixture of hematite, cuprospinel, tenorite and amorphous material. A reduction is required in order to change the phases to the active delafossite phase.

5.1 Hybrid Microwave Annealing

Different sizes of graphite crystals and powders were available for the HMA treatment. The different types of graphite mainly differed in heating homogeneity, final temperature and combustion rate. Various samples were microwaved and the visual appearance was used to get an indication of the homogeneity. The final temperature was determined using a combination of the brightness of the graphite hot spots and a thermal camera. The combustion rate was estimated by weighing the amount of graphite before and after several heat treatments. Table 5.1 shows the relative values of the different types of graphite.

A large size distribution of graphite crystals resulted in inhomogeneous heating and thereby reduced the reproducibility of the treatment. Fine graphite powder resulted in a homogeneous heating throughout the reaction set-up however the temperature was high and glass samples melted during the treatment. By compressing the graphite powder a more compact layer was formed which showed a lower amount of hot spots. As a result both the temperature and combustion rated lowered and the copper iron oxide was not reduced. A combination of compressed graphite with graphite powder was required

Table 5.1: Relative characteristics of different types of graphite

Graphite type	Heating Homogeneity	Combustion rate	Final temperature
Crystal mix	Low	Medium	Medium
Fine Crystals	Medium	Medium	High
Powder	High	High	High
Compressed Powder	High	Low	Low
Partial Compressed	High	Medium	Medium

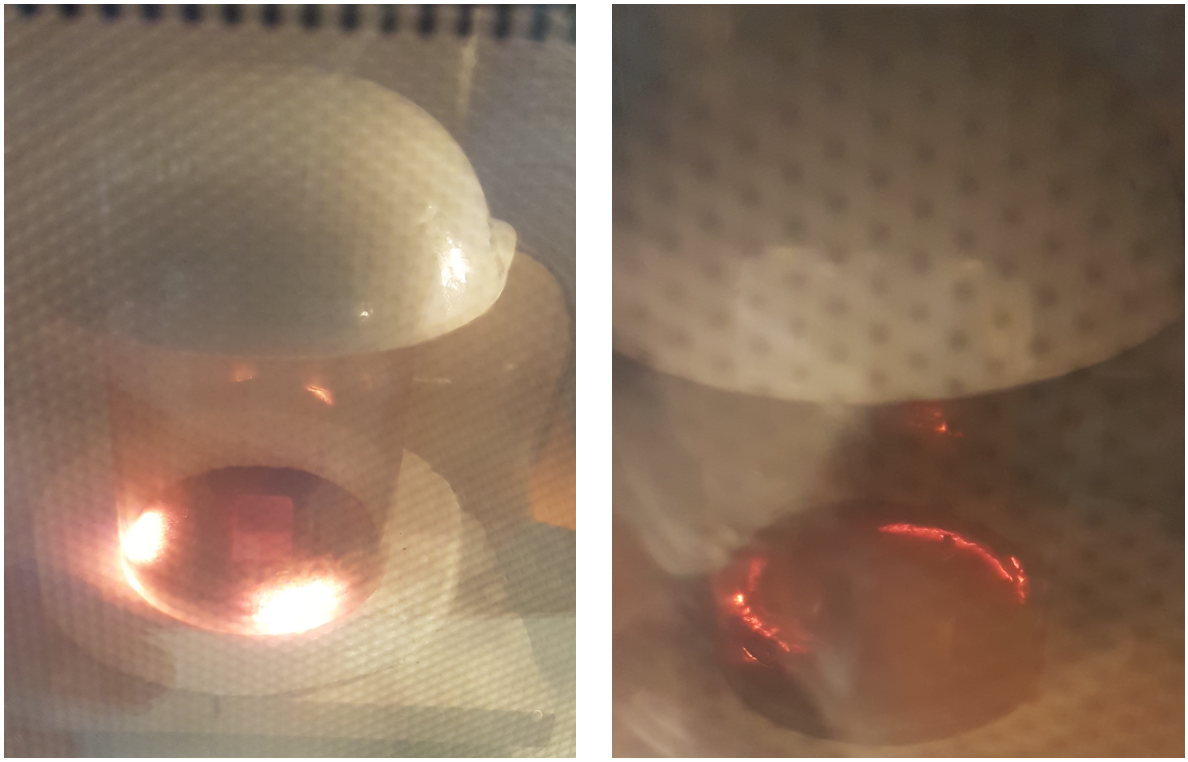

(a) Image showing intense hotspots **(b)** Image showing the final HMA set-up

Figure 5.1: Comparison between the a) the first HMA setup showing intense hotspots and b) the final HMA set-up showing a more homogenous heating pattern

to reach high enough temperature and combustion rate.

In order to gain a more precise control over the temperature and combustion rate various amounts of graphite were examined. 6 g to 12 g of different types of graphite were placed in the quartz beaker and microwaved for different times. The lower amounts of graphite interacted strongly with the microwave radiation and caused the samples to burn. On the contrary with large amounts of graphite the interaction was distributed which lowered the final temperature. The difference between using either small or large amounts of graphite can be seen in figure 5.2 The ideal amount of graphite for a good combustion rate and final temperature was found to be 7.5 g to 8.5 g.

Due to inhomogeneity in the commercial microwave some locations received intense microwave radiation and were heat quickly. Those locations have a high impact on the performance of the hybrid microwave radiation. When the HMA setup was placed directly in an intense area, the temperature quickly rose and causes the sample to either melt or burn. In order to find the most ideal spot for the microwave treatment the HMA set-up was placed in different locations.

The intense interaction caused by the concentrated microwave radiation resulted in partial heating of graphite to temperatures above 1500 °C. Those areas, called hot spots, were mainly located at the border of the HMA set-up. In order to increase the reproducibility the samples should be placed exactly between the hot spots and the alignment should be identical in each reaction. A displacement of a few millimeter significantly changed the outcome of the microwave and therefore great care was required for the sample placement.

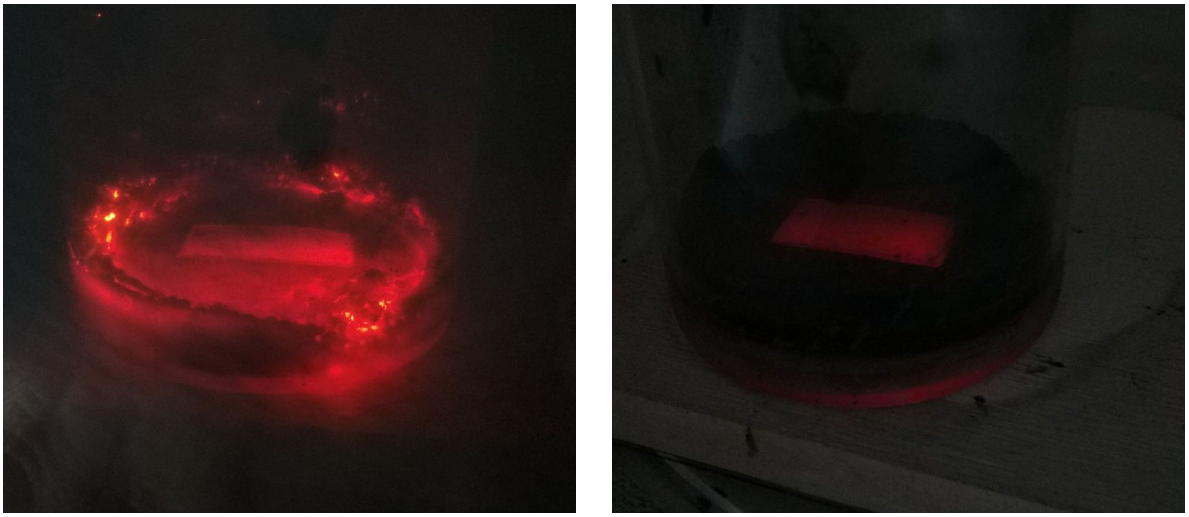

(a) **(b)**

Figure 5.2: Comparison between a) a small amount of graphite and b) a large amount of graphite

It is believed a low oxygen pressure contributes to the reduction of copper iron oxides. In order to prove the low oxygen pressure multiple experiments were conducted. The reduction was performed multiple times with and without closing the reaction chamber. A closed chamber frequently lead to reduction of the materials while an open chamber had no result or even reversed the reduction. In order to confirm the oxidation delafossite $CuFeO_2$ thin films were placed in the opened HMA set-up and treated for several minutes. In most cases this lead to oxidation to the cuprospinel $CuFe_2O_4$ crystal phase. After another treatment in a closed HMA set-up the delafossite $CuFeO_2$ was recovered. The second indication for the low oxygen pressure was the appearance of a blue flame when the set-up was opened quickly after the microwave treatment. Directly after the treatment graphite remains above 1000 °C for a brief moment at which spontaneous combustion occurs. The spontaneous combustion was only visible after opening the HMA set-up which indicates the absence of oxygen. The combination of the reversibility of the reaction and the spontaneous combustion of graphite lead us to conclude the oxygen in the HMA set-up is depleted during the microwave treatment.

Since the partial pressure of oxygen is of great importance different ways of influence were examined. The quartz beaker was closed using different types of lids unfortunately most lids reflected microwave radiation and thereby affected the reduction. Figure 2.4 shows the difference in heat created by two different ceramic bowls. The larger bowl clearly shows more black body radiation and therefore reached significantly higher temperatures which destroyed the samples. It was therefore chosen to use the second bowl and focus on other ways to influence the oxygen pressure. A second option was replacing the in the reaction chamber by argon gas to remove the oxygen and improve the reduction results. A positive effect was observed however a consistent reproducible result was not accomplished and it was chosen to use air as standard. The last option consisted of the application of silicon grease to seal the HMA set-up and thereby limit oxygen diffusion. The reduced oxygen diffusion lead to an improvement in the result while reducing the microwave time.

The last important parameter in hybrid microwave annealing is the time. The total reaction time can be divided in three areas namely the induction time, the combustion time and the reduction time. The induction time is the amount of time required to heat graphite until the spontaneous combustion starts. The combustion of graphite leads to a depletion of oxygen, the time it consumes is called the combustion time. Finally the reduction time is the time the sample requires to fully reduce to delafossite $CuFeO_2$. By fixing the amount graphite and the location of the set-up in the microwave the induction time is constant for each reaction. By properly closing the set-up the combustion time can be kept constant as well. The reduction time, however changes for each sample and mainly depends on the amount copper iron oxide and which crystal phases are present. The samples prepared with spray pyrolysis differ in crystallinity which complicates the microwave annealing therefore a heat treatment was introduced.

5.2 Oven treatment

In order to improve the crystallinity of the thin films an oven treatment was introduced. Different heating ramps, temperatures and annealing times were examined in order to find the best oven oven treatment. The main difference between a one hour and three hour ramp is visible in the physical appearance of the samples. A short heating ramp resulted in spot like damage to the surface of the sample which lead to a reduction in performance. Heat treating the samples with a 3 hour ramp did not lead to a difference in the XRD diagram, however it improved the performance of the thin films. A higher temperature increased the crystallinity however at longer times negatively influenced the performance. 600 °C is near the melting point of the glass transition of soda lime glass and the decrease in performance can be explained by tin diffusion into the thin film. Figure 5.3 shows an increase in crystallinity and a full conversion to the cuprospinel phase is reached after being heated to 550 °C for one hour. Heat treating for longer times did not result in a different XRD diagram, however it increased the performance slightly. All the results are summarized in table 5.2 and the best treatment has shown to be 550 °C for three hours using a three hour heating ramp.

Table 5.2: Results of combining various heating ramps and treatment times.

Temperature(°C)	Ramp(min)	Time(min)	XRD	Appearance	Performance
550	60	60	Medium	Spotlike	Low
550	180	60	Medium	Good	Medium
550	180	180	Good	Good	High
600	60	60	Medium	Spotlike	Low
600	180	60	Medium	Good	Medium
600	180	180	Good	Good	Medium

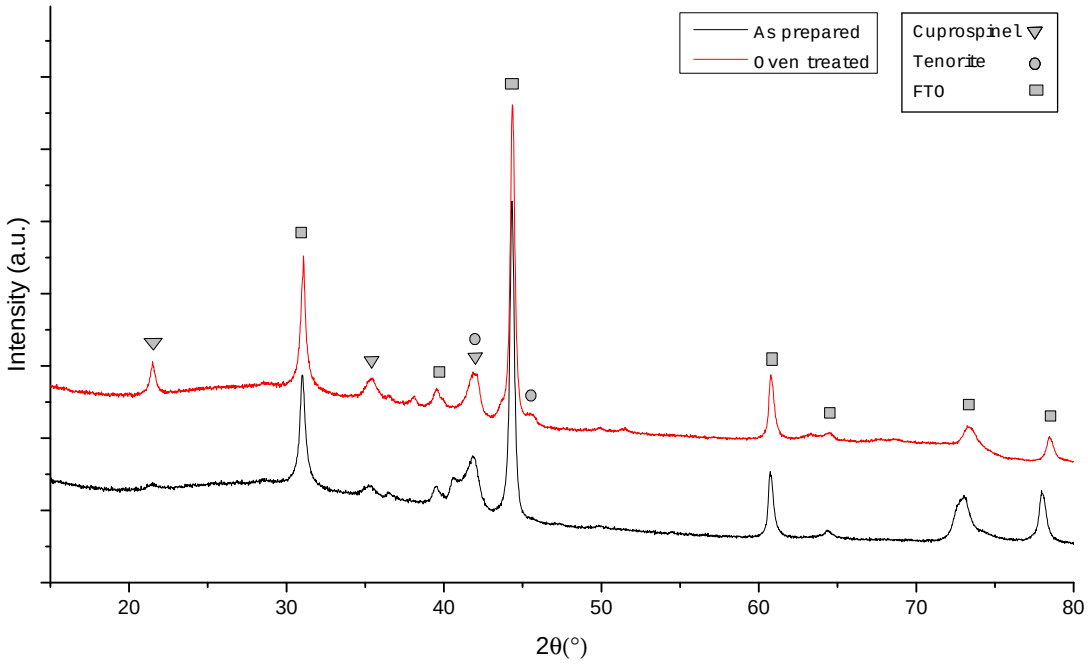

Figure 5.3: XRD diagram of copper iron oxide thin films as prepared and after a 1 hour oven treatment.

Chapter 6

Final Spray Pyrolysis Optimization

6.1 Temperature Effect

Previously it was shown a temperature of 450 °C resulted in higher quality films than 400 °C or lower. In order to get a better insight in the effect of the temperature reactions were repeated at 425 °C, 450 °C and 475 °C. Samples were analyzed using SEM and optical spectroscopy

6.2 Carrier Gas

Both N_2 and compressed air could be used as carrier gas for the deposition of $CuFeO_2$. In order to examine the influence two reactions were done. Both reactions used 80 mM iron, 34 mM copper, DMF, 450 °C and active nozzle cooling. The only difference difference being the carrier gas and the samples were analyzed with SEM imaging and the result is shown in figure 6.1. Samples prepared with air show more dark spots, indicating a more porous structure, and more nanostructured. Both will lead to increased surface area which could boost the performance significantly, however the stability of the nanostructured has shown to be lower than non-nanostructured samples. It was therefore chosen to continue using N_2 as carrier gas for the remaining reactions.

The flow rate of the carrier gas can be adjusted from $2\,\mathrm{L\,min^{-1}}$ to $10\,\mathrm{L\,min^{-1}}$, various samples were made using 2, 4, 6, or $10\,\mathrm{L\,min^{-1}}$. Samples were analyzed using XRD, optical spectroscopy and SEM. After the microwave treatment the XRD showed the delafossite phase present in all samples and a low to no presence of other phases. Both UV-VIS and SEM showed a large increase in thickness with a reduced flow rate, this can be explained by moving towards deposition regime C in figure 2.2 as explained in the theory. Furthermore the SEM images showed more nanostructered $CuFeO_2$ in the higher flow rate regimes. In order to have faster reactions and more stable, not nanostructured, thin films it was chosen to continue with the lowest flow rate of $2\,\mathrm{L\,min^{-1}}$.

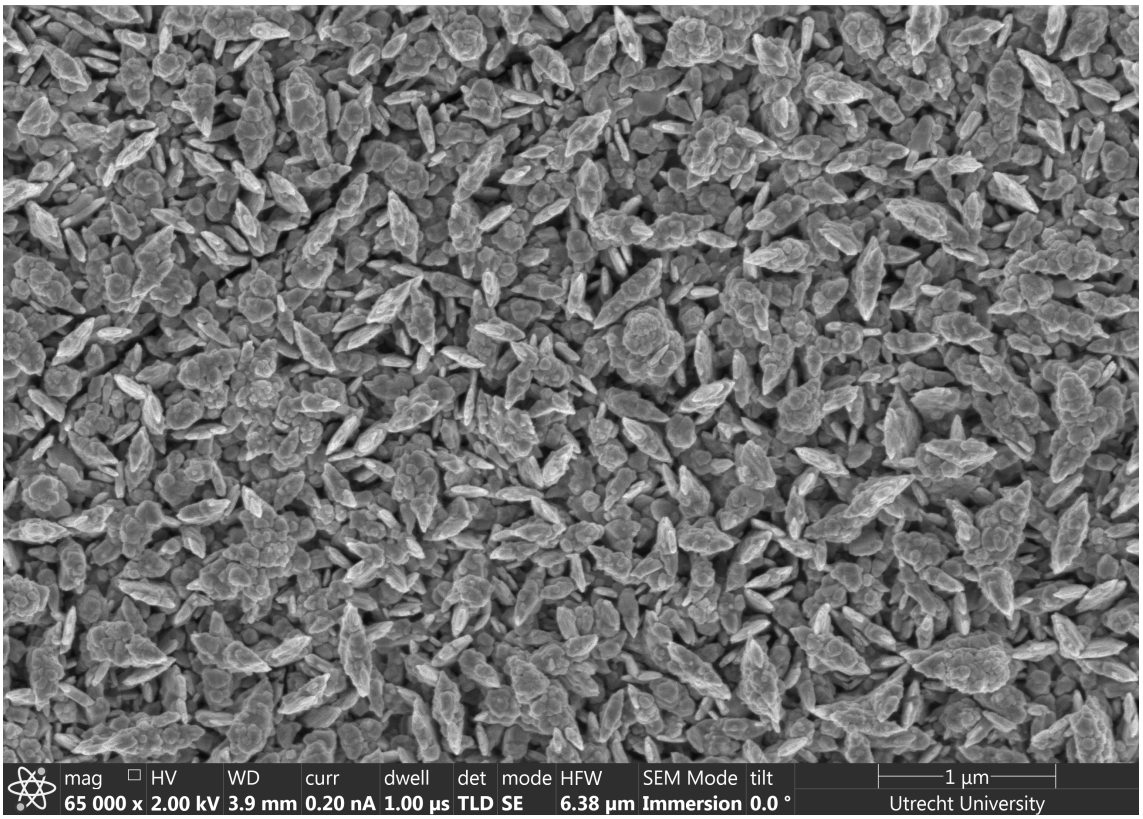

(a) air

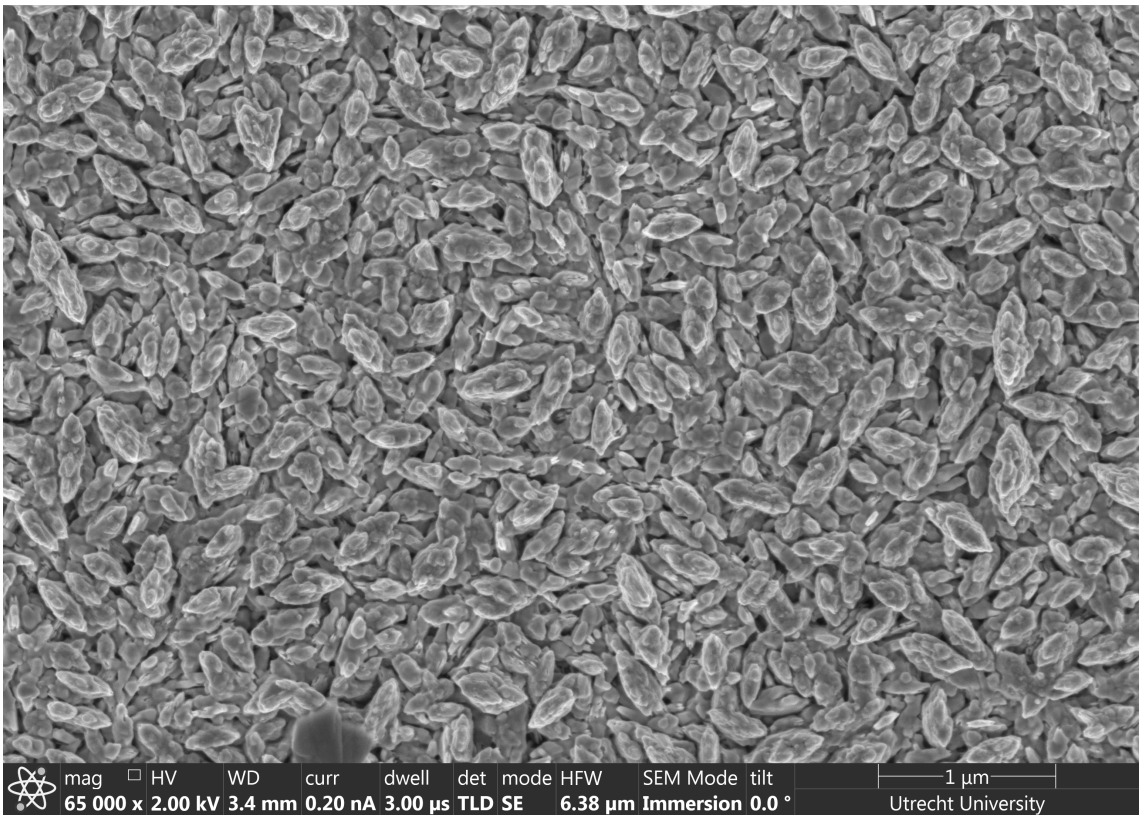

(b) N_2

Figure 6.1: Comparison between two SEM images of $CuFeO_2$ thin films prepared with air and N_2

6.3 Precursor Solution

Equal to the gas flow, the solution flow rate is an important parameter as well and be varied from $1\,\mathrm{mL\,min^{-1}}$ to $3\,\mathrm{mL\,min^{-1}}$. It was chosen to perform reactions under similar conditions while changing the solution flow rate from one to two and three milliliter per minute. Since the reactions are based on the deposition of a fixed amount of precursor solution the reaction time is inversely proportional to the solution flow rate. The deposition at $3\,\mathrm{mL\,min^{-1}}$ is three times as fast as the $1\,\mathrm{mL\,min^{-1}}$ thereby shifting to regime A in figure 2.2. As a result a rougher, more nanostructured surface arose since this was unfavorable for the stability of the thin films a reduced flow rate was required. Both one and two milliliter per minute resulted in flat, non nanostructured thin films. At $1\,\mathrm{mL\,min^{-1}}$ the samples were slightly thicker and therefore used the solution more efficiently, however it required the doubled amount of time as the $2\,\mathrm{mL\,min^{-1}}$. Since the results of both deposition rates were similar and the deposition required half the time, the $2\,\mathrm{mL\,min^{-1}}$ was chosen for further optimization.

6.4 Thickness Optimisation

Increasing the thickness leads to an increase in absorbance which boosts the performance, however the bulk recombination increases as well and will reduce the performance. Due to those counter affecting characteristics an optimal thickness, at which the performance is highest, can be found. Reactions using 10, 20, 30, 40, 50 and 60 milliL were performed under similar conditions, oven and microwave treated, the performance was compared using the PEC setup. As expected, the performance increases until a certain thickness and reduces again when the thickness is further increased. The 60 mL sample however, shows a large unexpected increase in performance and is therefore analyzed in more detail. Enlongated chronoamperometric measurements showed instabillity in the 60 mL sample which explained the higher initial current.

Chapter 7

Final Characterization

7.1 Material properties

The final optimized samples were thoroughly tested in order to confirm the characteristics of the material. UV-VIS spectroscopy was performed after reaction, after oven treatment and after the microwave treatment. Both the absorption and transmission spectra were recorded and are shown in figure 7.1 the transmission spectrum is used to make a tauc plot, see figure 7.2, to determine the direct and indirect bandgap. The direct bandgap was approximately 3.18 eV while the indirect band gap is approximately 1.39 eV both of which are in accordance to previous literature. The indirect bandgap is suitable for hydrogen evolution and can absorb solar radiation below 892 nm.

XRD measurements were performed to confirm the different phases present as prepared, oven treated and microwave treated. A combined diagram is shown in figure 7.3 and a clear change can be observed. As prepared the sample consists of a mix of phases and amorphous material, after the oven treatment the crystallinity increases and the oxidized $CuFe_2O_4$ cuprospinel phase increases. Next to cuprospinel a CuO tenorite phase is visible in the diagram. In both tenorite and cuprospinel copper is present as Cu(II) which must be reduced to Cu(I) in order to form the required delafossite $CuFeO_2$ phase. After the HMA treatment the peak around 20 2θ, assigned to cuprospinel, and the peaks assigned to tenorite dissapear completely and a new intense peak around 36 2θ arises together with various less intense signals at higher 2θ. All new peaks correlate with the reference diagram of delafossite $CuFeO_2$ and it can therefore be concluded that the microwave treatment completely converts the thin film to the required delafossite $CuFeO_2$ phase.

Scanning electron microscopy images of a 30 USP cycles photocathode after 550 °C and 3 min HMA are shown in Figure 7.4. The complete surface is free of pinholes or splashes with very conformal and macroporous morphology. From the inset of figure 7.4a, it was estimated that the average grain size was 136 nm ±12 nm. A FIB-SEM cross section of the sample (7.4b) shows the presence of macropores and good contact with the FTO substrate while the revealed thickness was 283 nm ±18 nm. Figure 7.5 shows that the as-prepared samples are dense and smoother, and only after the heat treatment for two hours and the HMA treatment, the grain growth leads to a macroporous morphology. This grain growth phenomena reduces the final surface area which might play a negative

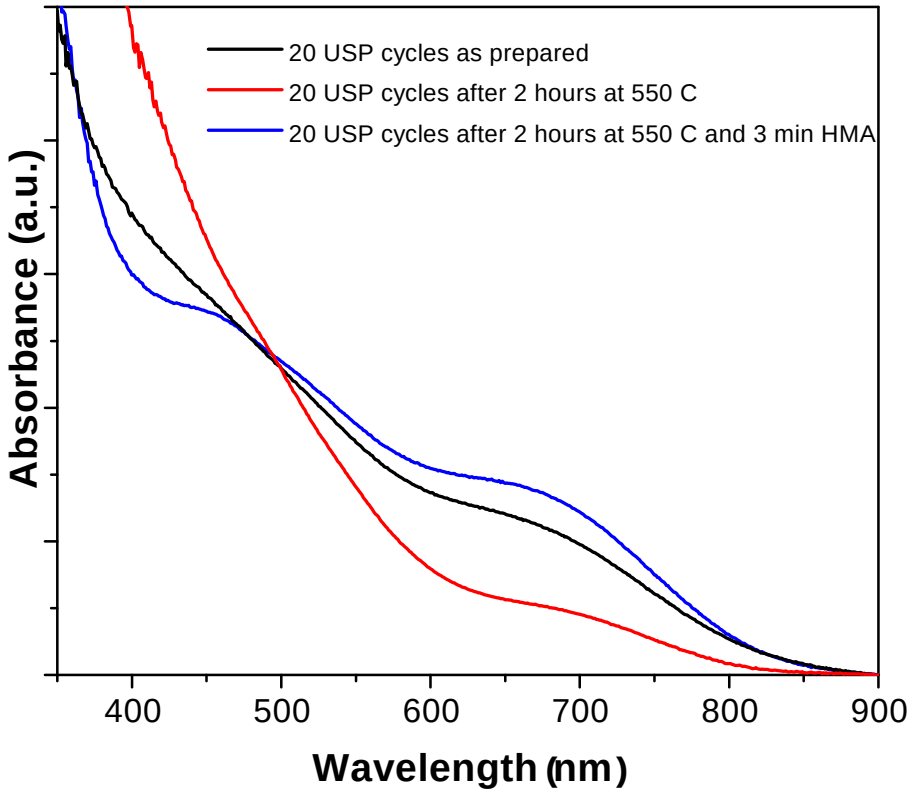

Figure 7.1: Absorption spectra of the same $CuFeO_2$ thin film as prepared, oven treated and microwave treated

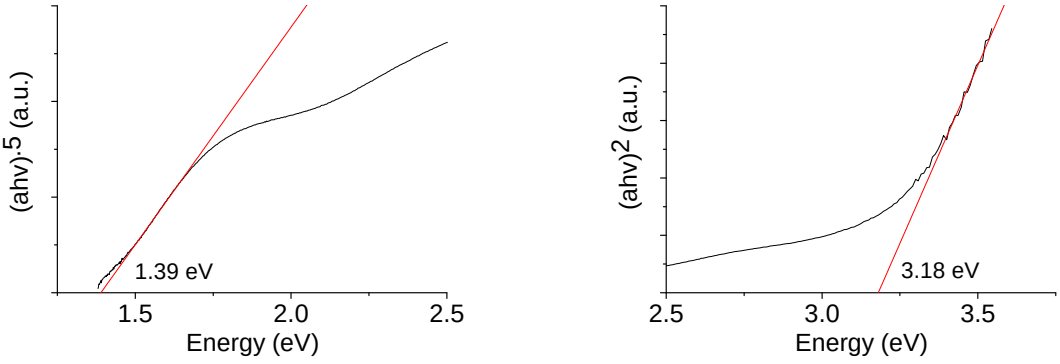

Figure 7.2: Tauc plots of the direct (a) and indirect (b) bandgap of delafossite $CuFeO_2$ thin film.

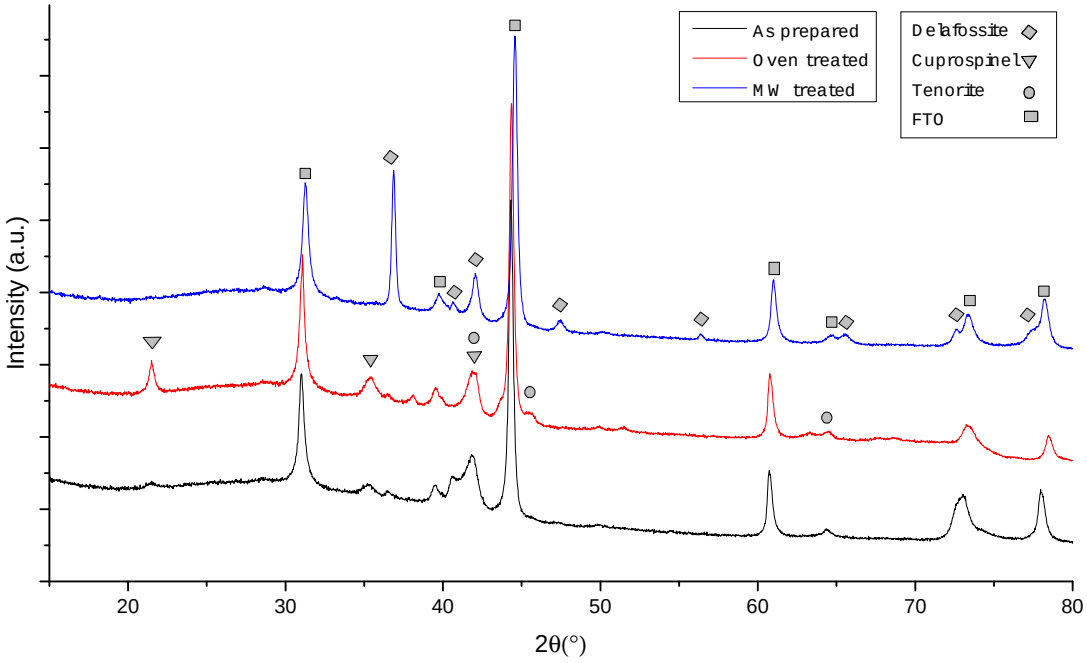

Figure 7.3: XRD diagram of a single sample as prepared, oven treated and microwave treated

effect in the performance.

To gain a further insight into the chemical and electronic properties of $CuFeO_2$ after preparation, heat treatment and HMA, we employed complementary X-ray absorption (XAS) and X-ray photoelectron (XPS) spectroscopy methods. Where XAS probes the unoccupied valence states of the Cu and Fe, and XPS probes the elemental composition and both the chemical and electronic state. The analysis of the iron L2,3- edge XAS spectra in $CuFeO_2$ during different preparation conditions showed that iron is present in the system as Fe(III) ([Ar]18 4s0 3d5]) and this oxidation state did not dramatically change upon the heat treatment or microwave treatment of the sample (figure 7.6a) [30]]. It is worth noting that the Fe XAS in this sample is very similar to that of Fe_2O_3 as both Fe_2O_3 and $CuFeO_2$ has similar crystal structure [31, 32].

On the other hand, The Cu L2,3- edge XAS showed that the oxidation state of copper in the as prepared and heat-treated samples is mainly Cu(II) ([Ar]18 4s0 3d9]) represented with an L3 and L2 edges at 931.5 eV and 953.5 eV (figure 7.6). The copper spectra of the freshly prepared and heat-treated samples also showed the presence of small quantity of Cu(I) ([Ar]18 4s0 3d10]). Quantification of this Cu(I) amount from the XAS spectra showed that they represent around 10% of the copper content in the sample. However, the Cu L2,3- edge XAS of the microwave-treated sample showed that around 90% of the Cu(II) was reduced to Cu(I), which clearly shows the effect of the short microwave treatment on the Cu reducibility. It is also noted that the feature at approximately 939 eV in the microwave treated sample is more pronounced than that in the freshly prepared and heat-treated samples, which indicates that this feature is more related to the Cu(I) unoccupied DOS rather than that of Cu(II). This feature is also present in the Cu0 XAS

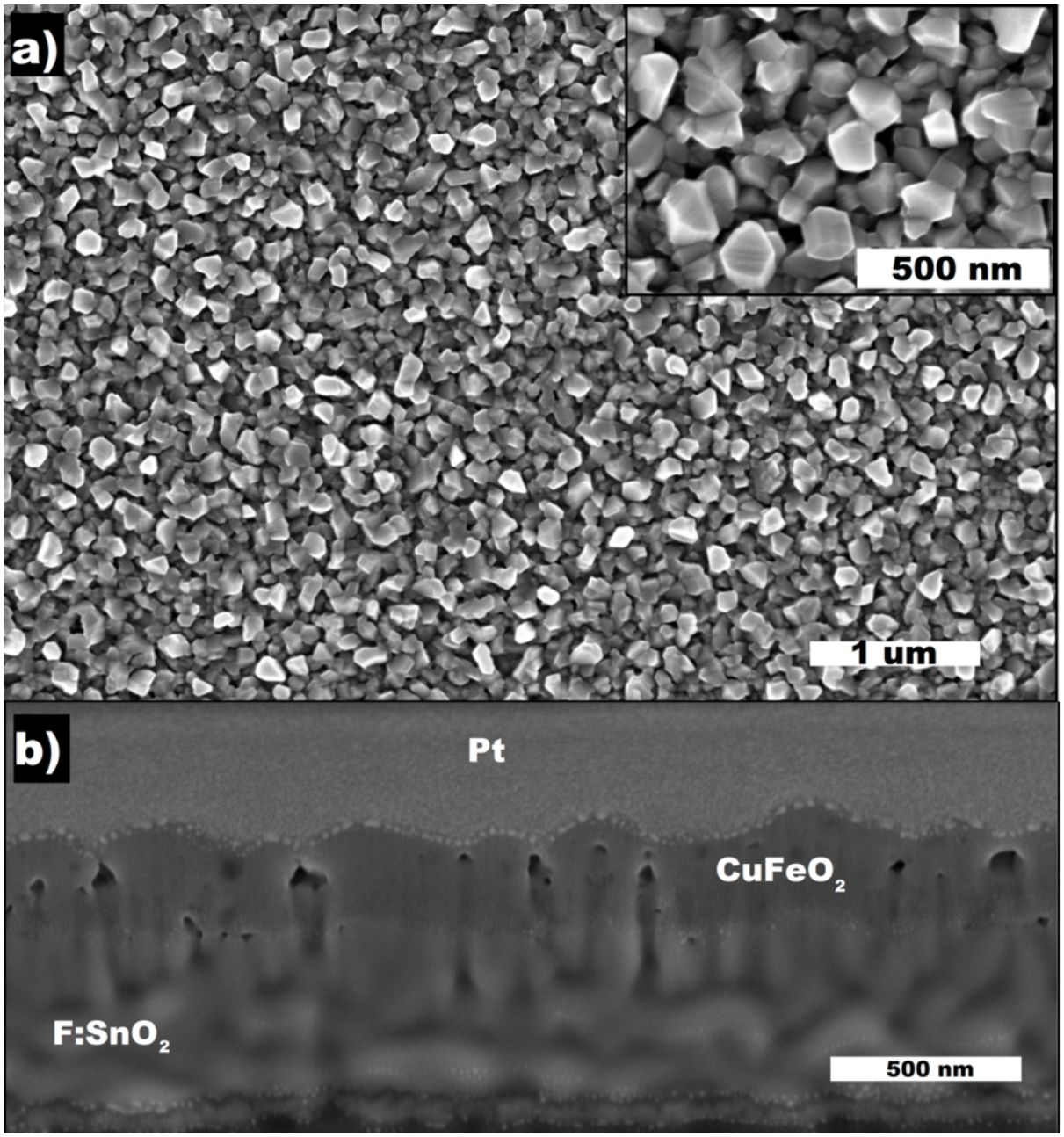

Figure 7.4: SEM images of a 30 USP cycles sample on FTO glass after heat treatment at 550 °C and 3 min HMA treatment. a) Top view and b) Focused Ion-Beam cross section.

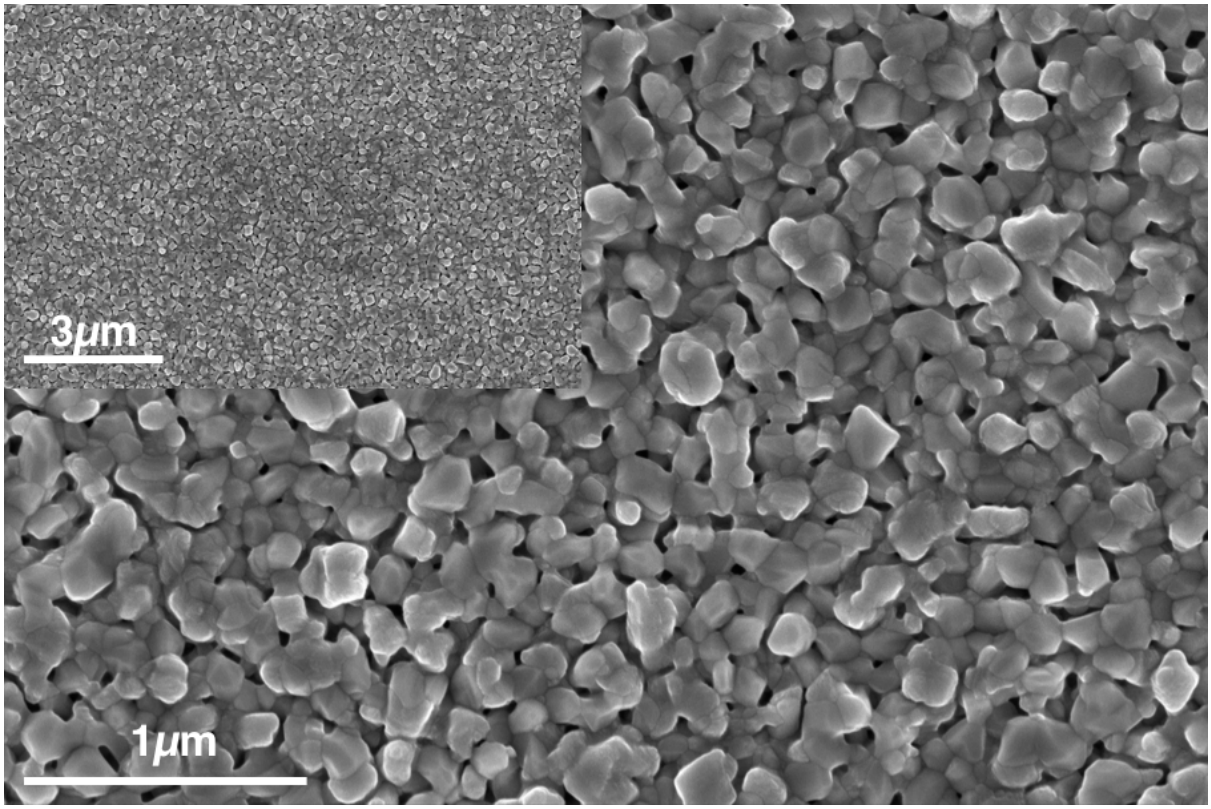

Figure 7.5: SEM images of a 30 USP cycles sample on FTO glass as prepared.

from M. Grioni et. al. [33], where they showed that the Cu(I) XAS contains features from both the Cu(II) and Cu0 spectra. Finally, as we recorded the XAS using total electron yield detection method, we estimated that the XAS probing depth of this experiment was around 2 nm, which probes the few $CuFeO_2$ layers below the surface [34].

In addition, we conducted XPS depth profiling at different excitation energies to probe the electronic properties of Fe, Cu, C and O at the surface (the top 1 nm) and compare this with their "bulk" electronic properties (at around 8 nm). The surface sensitive XPS was conducted at an excitation energy of 1.15 keV and showed that the Cu is always present as Cu(I) (recognizable by the doublet peaks at 932.6 eV and 952.4 eV) on the sample surface regardless of the type of treatment applied on the sample (figure 7.7). This observation is in agreement with the observation of M.S. Prevot et. al. [35].

Interestingly, the bulk-sensitive XPS was conducted on the same spot on the sample with an excitation energy of 5.93 keV (often referred to as HAXPES [36]) showed that copper is present in the freshly prepared and heat-treated samples as Cu(II) (recognizable by two satellite peaks of Cu 2p3/2 and Cu 2p5/2 at 942 eV and 961.7 eV respectively) while it was reduced to mainly Cu(I) by the effect of brief microwave treatment (figure 7.7). Iron on the other hand, remained always Fe(III) in the surface and bulk irrespective of the sample treatment which is in agreement with the observations from [10, 35] (figure 7.8).

Therefore, the XAS/XPS study we conducted on the $CuFeO_2$ sample showed that iron was always present as Fe(III) in the surface and bulk of the sample, while copper was present as mainly Cu(II) in the bulk and then was reduced to Cu(I) under the influence of microwave treatment, which confirms that a short microwave treatment of the sample transformed

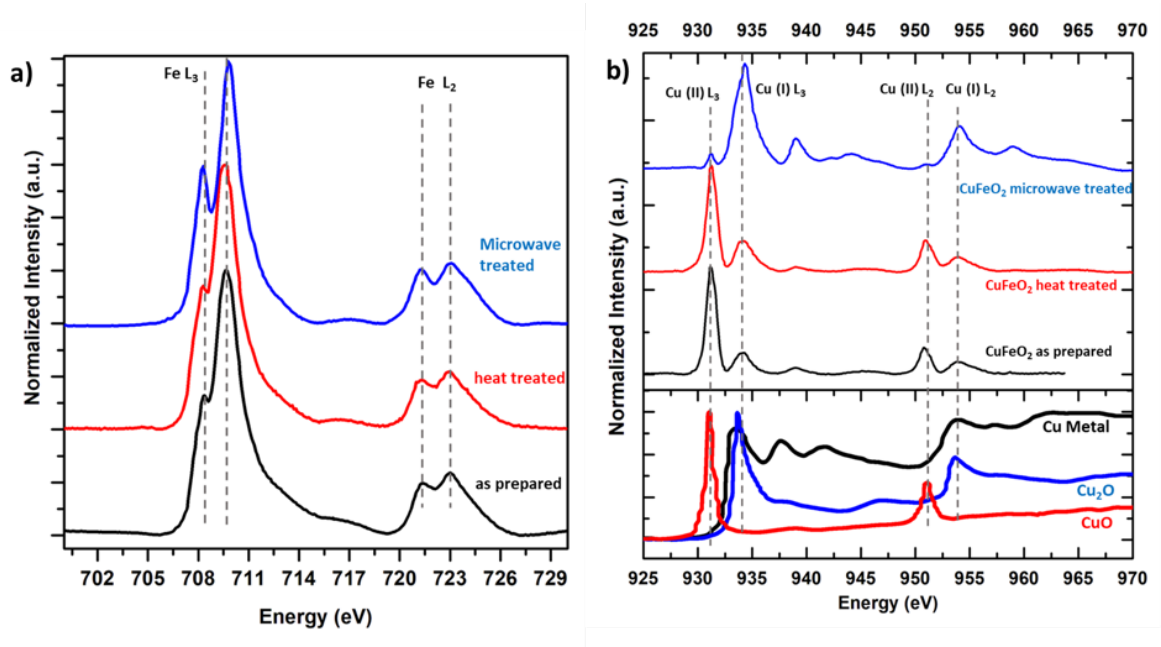

Figure 7.6: a) Fe 2p XAS and b) Cu 2p XAS profiles of $CuFeO_2$ after preparation, thermal treatment and microwave treatment. The copper reference spectra have been adapted from [34]

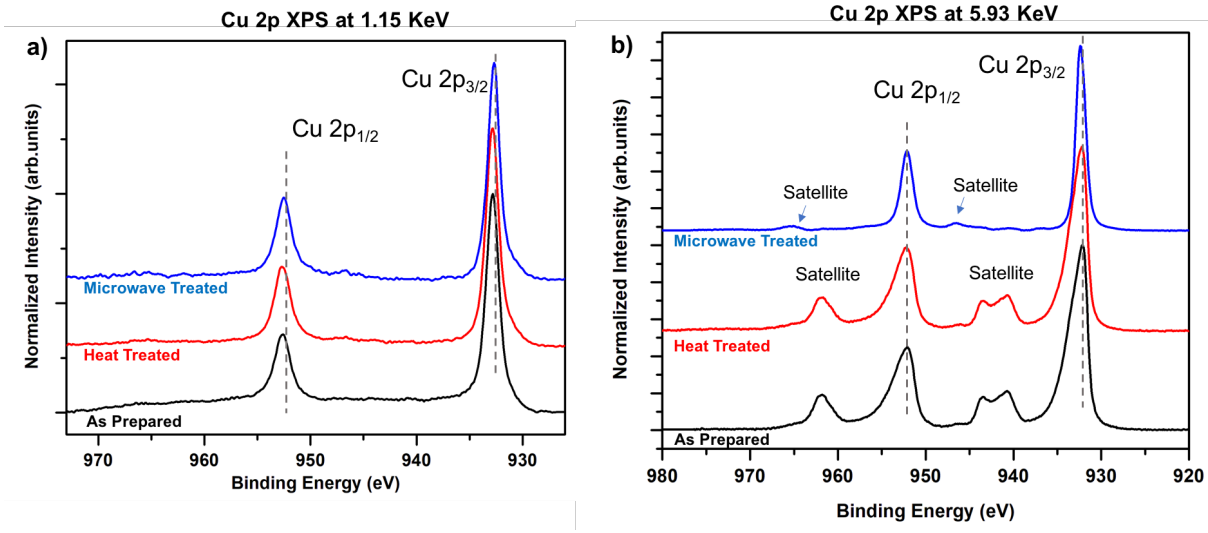

Figure 7.7: Cu 2p XPS at 1.15 KeV excitation energy and b) Cu 2p XPSat 5.93 KeV excitation energy in CuFeO2 after preparation, thermal treatment and microwave treatment

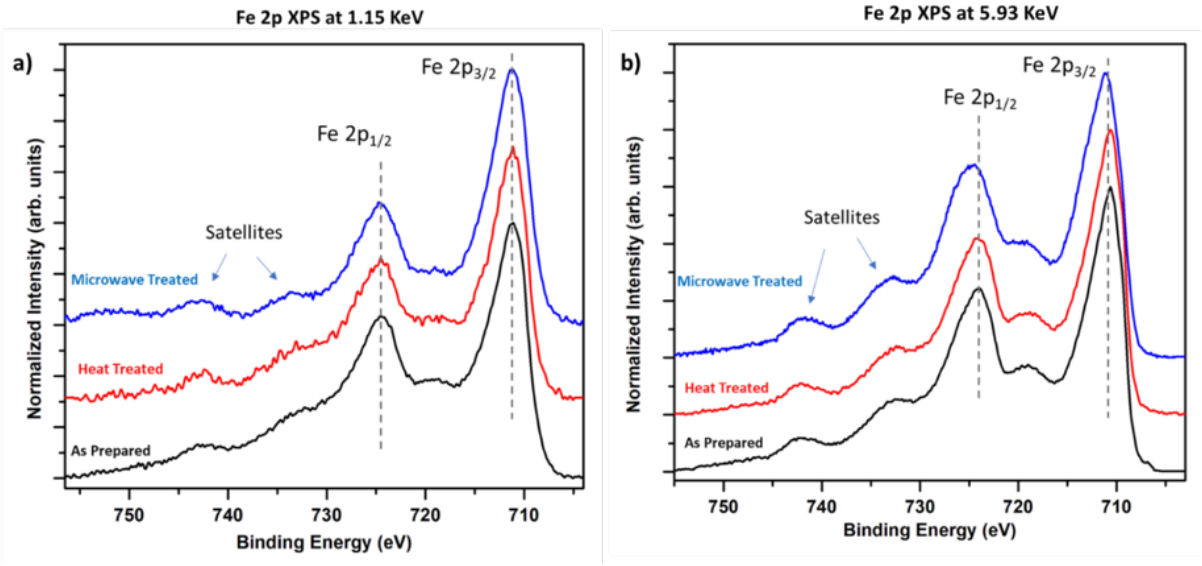

Figure 7.8: Fe 2p XPS at 1.15 KeV excitation energy and b) Fe 2p XPS at 5.93 KeV excitation energy in $CuFeO_2$ as prepared, thermal treatment and microwave treatment.

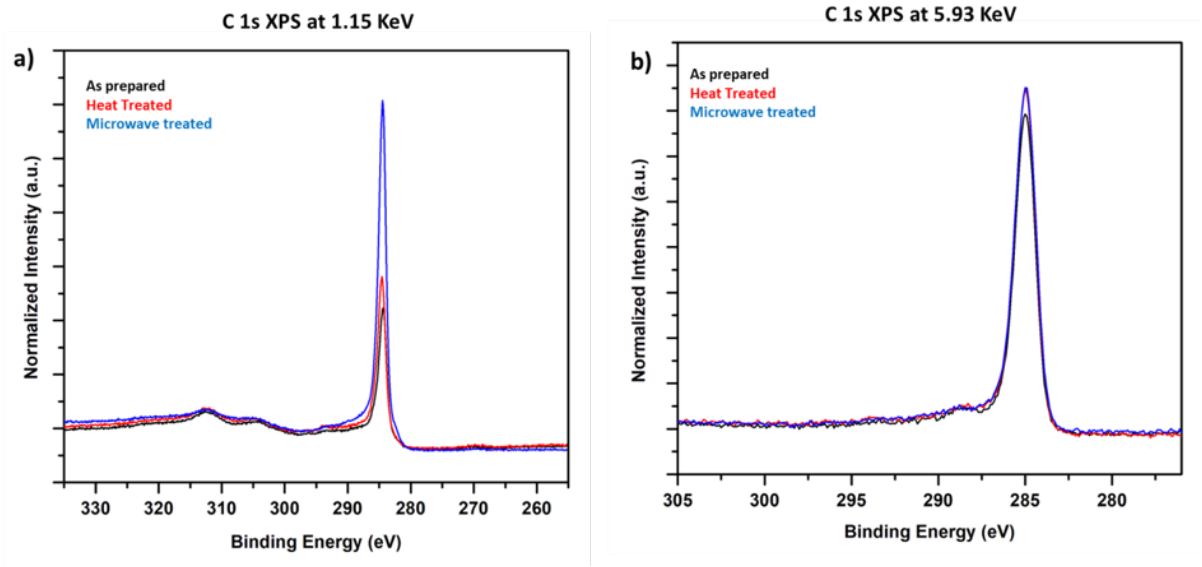

Figure 7.9: C 1s XPS at 1.15 KeV and b) at 5.93 KeV excitation energy in CuFeO2 after preparation, thermal treatment and microwave treatment.

the CuO : Fe_2O_3 to the delafossite $CuFeO_2$ phase. On the sample surface, copper was permanently present as Cu(I) irrespective of the sample treatment procedures.

Finally, carbon 1S XPS investigation showed that carbon was present extensively on the samples surface after microwave treatment in comparison with its presence in the fresh and heat-treated sample (figure 7.9). Nevertheless, its concentration did not show a significant change in the bulk after microwave treatment. This finding may give an important indication on the stability of the Cu(I) at the surface as it is possible that some sort of a relatively carbon-rich phase is formed at the surface (carbide or carbonyl) during microwave treatment that may have an effect on the Cu oxidation state as well as in the photoelectrochemical activity of $CuFeO_2$ photocathodes.

7.2 Photoelectrochemical performance

In order to characterize the photoelectrochemical activity and stability of the resulting photocathodes, the optimized HMA treated samples were placed in a home-made teflon photoelectrochemical cell (PEC) fitted with an optical grade quartz window and filled with 140 mL of a 1 M NaOH solution. A Pt coil was employed as the counter electrode and a saturated Ag/AgCl electrode as reference. The solar simulated illumination was provided by a Hamamatsu 75 W Xenon arc lamp with a 1.5 AM filter and calibrated to 100 mW cm^{-2}. It was reported that $CuFeO_2$ delafossite photocades prepared by sol-gel and annealed in Ar at 700 °C, show negligible activities towards the hydrogen evolution reaction (HER) [4]. Therefore, the oxygen reduction reaction is used as a reference reaction to compare the performance of the thin films. Continues O_2 bubbling is used to saturate the sodium hydroxide with oxygen and allow for a constant oxygen concentration. In order to confirm the performance is due to O_2 reduction, a second measurement is performed under Ar bubbling which results in oxygen depleted solution.

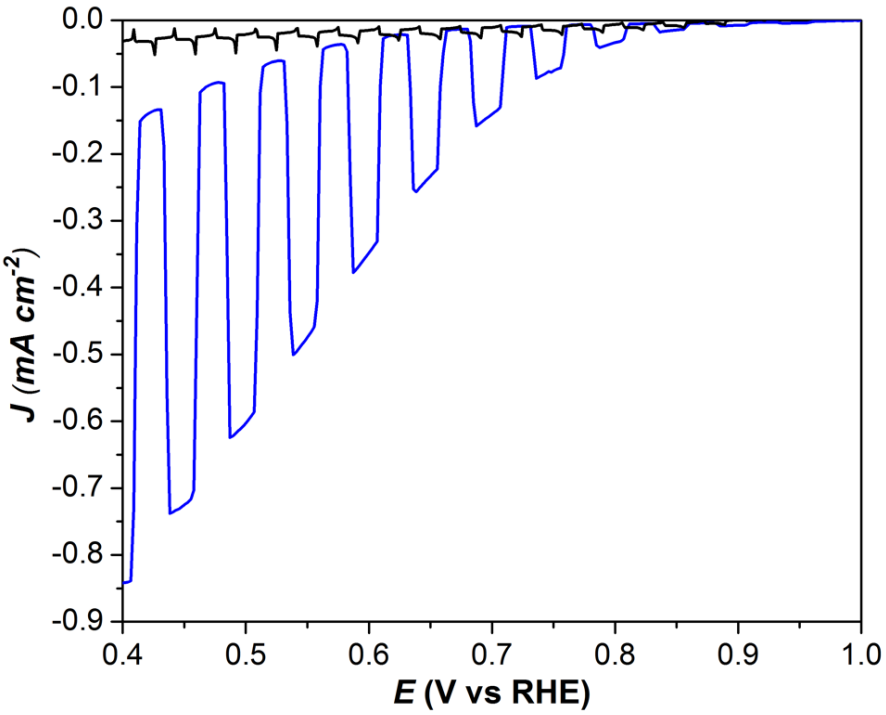

Figure 7.10: Chopped light linear sweep voltammetry in the cathodic direction of a 30 USP cycles photoelectrode after heat treatment for 2 hours and HMA for 3 min, in a 1 M NaOH solution saturated with O_2 (blue line) and saturated with Ar (black line). The scan rate was 10 mV/ sec and the sample was illuminated from the front. The inset represents the relation between the number of USP cycles versus the film thickness and photocurrent at 0.4 V vs RHE.

Our results are in agreement with the reported values as shown in the sweep voltametries in figure 7.10. Where a 30 USP cycles photocathode was intermittently illuminated from the front (electrolyte/film junction) in the O_2 saturated solution (blue line) and an Ar saturated solution (black line). Clearly, in the absence of a sacrificial agent low photocurrents in the order of 10 µA cm^{-2} indicate that there is no evolution of H_2. In the saturated solution a maximum photocurrent of about 650 mA cm^{-2} was found for the 30 USP cycles thin film at 0.4 V vs RHE.

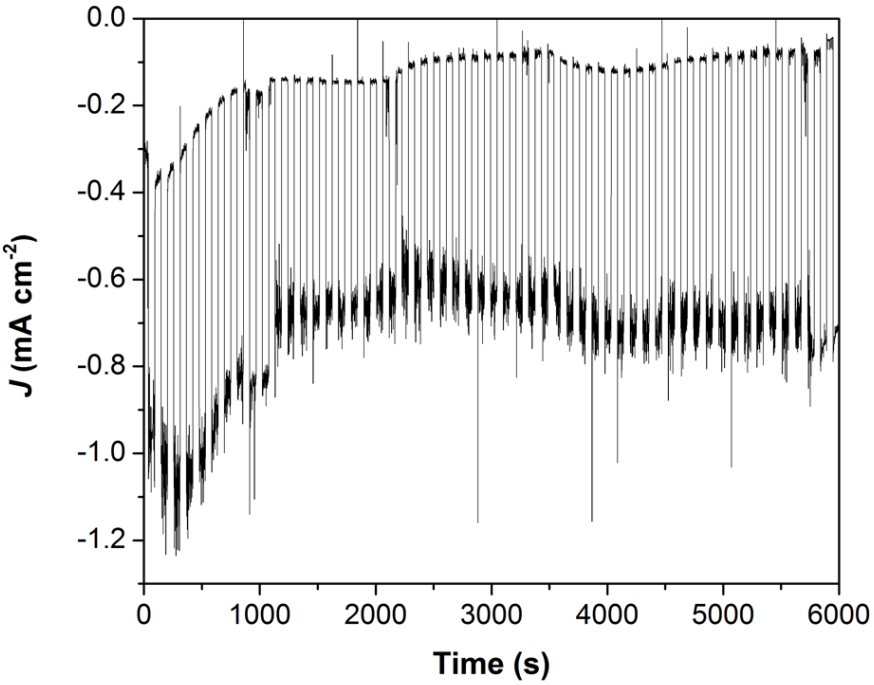

Figure 7.11: Chronoamperometry of a bare 30 USP cycles $CuFeO_2$ photocathode at 0.4 V vs RHE in a 1 M NaOH solution with strong O_2 bubbling under chopped 1.5 AM simulated illumination.

In order to confirm the stability of the samples a chronoamperometry under O_2 bubbling and on/off cycles of 55 seconds each was performed. Figure 7.11 shows the stability of a 30 USP cycles photocathode polarized at 0.4 V vs RHE during 6000 s. A minor degradation occurring in the first 20 minutes can be observed which could be explained by removal of the Cu metal species found with the XAS measurements. After 20 minutes minor fluctuations in both the dark and light current can be observed which are related to the inconsistent O_2 supply. No further noticeable changes occur over the remaining 80 minutes and therefore the stability of the photocathode is confirmed.

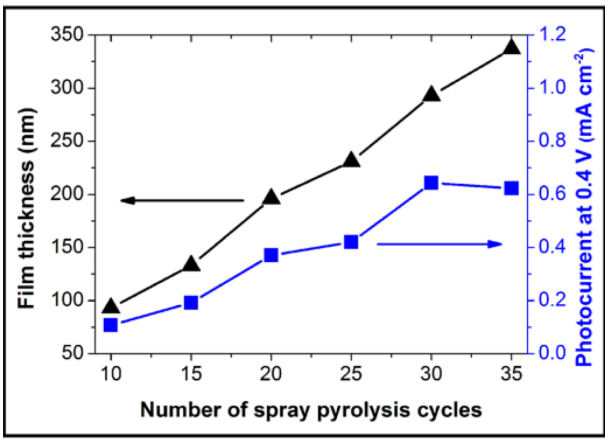

Figure 7.12: Thickness optimisation showing the correlation between the amount of USP cycles with the resulting FIB-SEM crossection thickness and the with chronoamperometry determined photocurrent

In order to further optimize the thickness chronoamperometry measurements were performed on samples made with 10 to 35 USP cycles after which the thickness was measured by making a FIB-SEM crossection. Figure 7.12 shows the correlation of the thickness and number of USP cycles together with the observed photocurrents. Thicknesses beyond 300 nm seem to start showing a detrimental effect in the performance and therefore 30 USP cycles, resulting in 290 nm, performed best.

Chapter 8

Conclusions

The absorption and emission spectra combined with the XRD diagram, SEM-EDX and ICP combined show a successful three-step synthesis of delefossite $CuFeO_2$ photocathodes. The first step, ultrasonic spray pyrolysis, performed best with $Fe(acac)_3$ and $Cu(NO_3)_2$ in DMF at 450 °C. Reaction times were significantly reduced by increasing the iron and copper concentrations to 80 mM and 34 mM respectively. The resulting atomic ratio of copper and iron in the thin film photocathodes was estimated by using EDX and ICP. However, additional ICP measurements are required to confirm the final atomic ratio.

XRD measurements showed that the second step in the reaction, the heat treatment at 550 °C for two hours, significantly increases the crystallinity and thereby improves the stability. During the treatment the photocathode is fully oxidized to Cu(II) present in a cuprospinel or tenorite phase.

During the HMA a full conversion to the required delafossite $CuFeO_2$ phase was observed within 10 minutes depending on the thickness of the thin film and the amount of graphite used during the treatment. The effect of microwave radiation was confirmed by doing similar experiment in a muffle-oven without the aid of microwave radiation. The combined effect of heat, graphite combustion, a low oxygen pressure and a change in the di-electric loss constant resulted in an ultra-fast structure change within 10 minutes.

The final optimized delafossite $CuFeO_2$ photocathodes were thoroughly analyzed after each step the reaction. The stoichiometric ratio of copper and iron was estimated using SEM-EDX and ICP and found to have a slight excess of iron. Using a Tauc calculation the direct and indirect bandgap are estimated on 3.18 eV and 1.39 eV respectively. XRD patterns showed a mix of phases directly after deposition, full oxidation to cuprospinel $CuFe_2O_4$ after the heat treatment and a full conversion to delafossite $CuFeO_2$ after the HMA treatment. PEC tests were performed to determine the performance and optimal thickness of the resulting photocathodes. 30 USP cycles resulted in approximately 290 nm thickness and 0.644 mA cm^{-2} photocurrent which is about half of previously reported photocurrents. Which could be caused by the presence of Cu metal, the high carbon content in the HMA treated photocathodes or the lower surface area compared to the literature.

Previously reported sol-gel methods required approximately 10 h to form the thin film with highest performance while 30 USP cycles requires approximately 1 h and therefore

USP results in a ten fold decrease in preparation time. Reaction time is even more reduced by the HMA annealing method which takes about 10 min instead of a 6 h heat treatment under argon atmosphere. The oven treatment to improve the stability does require two hours however, the total reaction is still reduced approximately eight times. The combination of shorter duration, less heating and the use of ambient atmospheres have lead to a significant increase in the cost efficiency of the delafossite $CuFeO_2$ photocathode.

Chapter 9

Outlook

Since the performance is about half of previously reported the thin film synthesis can even be improved with a future project. The main difference with the previously reported samples is the nanostructure which significantly increases the surface area and thereby the performance of the thin film. Nanostructured copper iron oxide thin films with USP can easily be accomplished however, it complicates the HMA treatment step. Due to the complicated mechanism of the HMA step it was not possible to fully convert to the required delafossite $CuFeO_2$ phase which led to instability during the PEC tests. In order to improve the HMA results a dedicated laboratory microwave should be used instead a commercial microwave to gain a more controlled treatment and reach full conversion.

Next to the different treatment, the HMA setup should be improved as well. XPS measurements have shown a large increase in the carbon content after the HMA treatment which is believed to have a negative effect on the performance. Using an industrial microwave in combination with an industrial grade HMA cell showed in figure 2.3 will lead to more controlled reaction and will reduce the probability of carbon contamination.

A second improvement in performance could be achieved by the use of dopants. Several treatments like intercelation of oxygen, doping with nitrogen or magnesium have already shown an increase in performance in delafossite materials and could improve the performance of the photocathode. After the final optimization the efficiency of the photocathode can be determined with incident photon to current efficiency measurements. A next step would be investigating the deposition of a hydrogen evolution catalyst platinum or nickel/molybdenum and determining the incident photon to hydrogen efficiency.

At last the fully optimized photocathode can be combined with the hematite Fe_2O_3 photoanode and placed in the photoelectrochemical tandem cell.

Acknowledgements

With this I would like to sincerely thank Iván Garcia Torregrosa (PhD cnadidate) for guiding me from day to day, explaining me new techniques like spray pyrolysis and hybrid microwave annealing, and lecturing me about material science and photoelectro chemistry. Next to the teaching I would like to thank Ivan for the day to day talks and laughs and making sure I had a great time at the lab.

I would like to thank Ahmed S.M. Ismail (PhD candidate) for the weekly talks and helping me with the XAS and XPS measurements.

I would like to thank dr. Florian Meirer and prof. dr. ir. Bert M. Weckhuysen for giving me this project, guiding throughout the thesis and giving feedback on the presentation.

I would like to thank the Solar Fuels group for the support during the project, the monthly meetings and for giving new ideas for the project.

I would like to thank the technical staff for allowing me and helping me with building all the setups I required during my thesis.

At last I would like to thank the inorganic chemistry and catalysis group for a very nice time.

Bibliography

(1) CBS Nederland voorlaatste op ranglijst EU hernieuwbare energie., 2016.
(2) CBS Windenergie; elektriciteitsproductie, capaciteit en windaanbod per maand., 2017.
(3) Sivula, K.; van de Krol, R. *Nature Reviews Materials* **2016**, 16010.
(4) Prévot, M. S.; Guijarro, N.; Sivula, K. *ChemSusChem* **2015**, *8*, 1359-1367.
(5) Prévot, M. S.; Guijarro, N.; Sivula, K. *ChemSusChem* **2015**, *8*, 1359-1367.
(6) Prevot, M. S.; Li, Y.; Guijarro, N.; Sivula, K. *Journal of Materials Chemistry A* **2016**, *4*, 3018-3026.
(7) Koffyberg, F. P.; Benko, F. *Physical Chemistry* **1987**, *35*, 8207-8214.
(8) Morrison, S. R., *Electrochemistry at Semiconductor and Oxidized Metal Electrodes*; Plenum Press: New York: 1980, p 137.
(9) Chen, H. Y.; Wu, J. H. *Thin Solid Films* **2012**, *520*, 5029-5035.
(10) Jang, Y. J.; Park, Y. B.; Kim, H. E.; Choi, Y. H.; Choi, S. H.; Lee, J. S. **2016**.
(11) Chen, H. Y.; Wu, J. H. *Applied Surface Science* **2012**, *258*, 4844-4847.
(12) Willemars, J.; Torregrosa, I. G.; Barroso, M. Synthesis, Characterisation and Optimisation of $CuFeO_2$ Photocathodes for Water Splitting., Ph.D. Thesis, Utrecht, 2015, 1-12.
(13) Omeiri, S.; Gabes, Y.; Bouguelia, A.; Trari, M. *Journal of Electroanalytical Chemistry* **2008**, *614*, 31-40.
(14) Barnabé, A.; Mugnier, E.; Presmanes, L.; Tailhades, P. *Materials Letters* **2006**, *60*, 3468-3470.
(15) Thahab, S. M.; Alkhayatt, A. H. O.; Zgair, I. A. *Materials Science in Semiconductor Processing* **2016**, *41*, 436-440.
(16) Gu, J.; Wuttig, A.; Krizan, J. W.; Hu, Y.; Detweiler, Z. M.; Cava, R. J.; Bocarsly, A. B. **2013**.
(17) Chen, H. Y.; Fu, J. R. *Materials Letters* **2014**, *120*, 47-49.
(18) Read, C. G.; Park, Y.; Choi, K. S. *The Journal of Physical Chemistry Letters* **2012**, *3*, 1872-1876.
(19) Bhattacharya, M.; Basak, T. *Energy* **2016**, *97*, 306-338.
(20) Kelly, A. J. *Aerosol Science and Technology* **1990**, *12*, 526-537.
(21) Kumar, A.; Zhou, C. *American Chemical Society* **2010**, *4*, 11-14.
(22) Balanis, C. A., *Advanced Engineering electromagnetics*; Wiley: 2012, p 1045.
(23) Hippel, A. V., *Dielectrics and waves*; Wiley: New York, NY, 1966; Vol. 1, 1-294.
(24) Banyamin, Z.; Kelly, P.; West, G.; Boardman, J. *Coatings* **2014**, *4*, 732-746.
(25) Walkiewicz, J.; Kazonich, G.; McGill, S. **Feb. 1988**, *5*, 39-42.
(26) Giangrandi, I. Giangrandi., 2013.
(27) Xiaowei, L.; Jean- Charles, R.; Suyuan, Y. *Nuclear Engineering and Design* **2004**, *227*, 273-280.

(28) Tauc, J. *Materials Research Bulletin* **1968**, *3*, 37-46.
(29) Noh, H. J.; Jeong, J.; Chang, B.; Jeong, D.; Moon, H. S.; Cho, E. J.; Ok, J. M.; Kim, J. S.; Kim, K.; Min, B. I.; Lee, H. K.; Kim, J. Y.; Park, B. G.; Kim, H. D.; Lee, S. *Scientific Reports* **2014**, *4*, 2-7.
(30) Miedema, P. S.; De Groot, F. M. *Journal of Electron Spectroscopy and Related Phenomena* **2013**, *187*, 32-48.
(31) Grau- Crespo, R.; Al- Baitai, A. Y.; Saadoune, I.; De Leeuw, N. H. *Journal of Physics Condensed Matter* **2010**, *22*.
(32) Galakhov, V. R.; Poteryaev, a. I.; Kurmaev, E. Z.; Anisimov, V. I.; Bartkowski, S.; Neumann, M.; Lu, Z. W.; Klein, B. M.; Zhao, T. R. *Phys. Rev. B* **1997**, *56*, 4584-4591.
(33) Grioni, M.; Goedkoop, J. B.; Schoorl, R.; de Groot, F. M. F.; Fuggle, J. C. *Physical review B* **1989**, *39*, 1541-1545.
(34) Abbate, M.; Goedkoop, J. B.; de Groot, F. M. F.; Grioni, M.; Fuggle, J. C.; Hofmann, S.; Petersen, H.; Sacchi, M. *Surface and Interface Analysis* **Jan. 1992**, *18*, 65-69.
(35) Prévot, M. S.; Jeanbourquin, X. A.; Bourée, W. S.; Abdi, F.; Friedrich, D.; van de Krol, R.; Guijarro, N.; Le Formal, F.; Sivula, K. *Chemistry of Materials* **2017**, *29*, 4952-4962.
(36) Mudd, J. J.; Lee, T. L.; Muñoz- Sanjosé, V.; Zúñiga- Pérez, J.; Hesp, D.; Kahk, J. M.; Payne, D. J.; Egdell, R. G.; McConville, C. F. *Physical Review B* **2014**, *89*, 035203.
(37) Sabnis, S. M.; Bhadane, P. A.; Kulkarni, P. G. *Journal of Applied Physics* **2013**, *4*, 7-11.
(38) Lim, S. H.; Desu, S.; Rastogi, A. C. *Journal of Physics and Chemistry of Solids* **2008**, *69*, 2047-2056.
(39) Snyders, C. D.; Ferg, E. E.; Schuelein, J.; Loewe, H. **2016**, 88-97.
(40) Li, Y.; Li, X.; Wang, Z.; Guo, H.; Li, T. *Journal of Alloys and Compounds* **2017**, *696*, 836-843.
(41) Sirks, B. **2015**.
(42) Filipovic, L. Topography Simulation of Processing Techniques.
(43) Geertzema, Y. G. **2017**, 3018.
(44) Tauc, J.; Grigorovici, R.; Vancu, A. Optical Properties and Electronic Structure of Amorphous Germanium., 1966.
(45) Kaya, I. C.; Sevindik, M. A.; Akyildiz, H. **2016**, 2404-2411.
(46) Saravanan, V.; Shankar, P.; Mani, G. K.; Rayappan, J. B. B. *Journal of Analytical and Applied Pyrolysis* **2015**, *111*, 272-277.
(47) Keijzer, P. **2016**.
(48) Walter, M. G.; Warren, E. L.; McKone, J. R.; Boettcher, S. W.; Mi, Q.; Santori, E. A.; Lewis, N. S. *Chemical Reviews (Washington, DC, United States)* **2010**, *110*, 6446-6473.
(49) Wei, R.; Tang, X.; Hu, L.; Yang, J.; Zhu, X.; Song, W.; Dai, J.; Xuebin, Z.; Sun, Y. *Journal of Materials Chemistry C* **2017**, *5*, 1885-1892.
(50) Xu, Y.; Nie, G. z.; Zou, D.; Tang, J. w.; Ao, Z. *Physics Letters A* **2016**, *380*, 3861-3865.
(51) Pabst, A. **1937**, *303*, 539-546.
(52) Prevot, M. S.; Sivula, K. **2013**.

(53) Chen, Z.; Deutsch, T. G.; Dinh, H. N.; Domen, K.; Emery, K.; Forman, A. J.; Gaillard, N.; Garland, R.; Heske, C.; Jaramillo, T. F.; Kleiman- Shwarsctein, A.; Miller, E.; Takanabe, K.; Turner, J. In *Photoelectrochemical Water Splitting: Standards, Experimental Methods, and Protocols*; Springer New York: New York, NY, 2013, 87-97.
(54) Lamri Zeggar, M.; Chabane, L.; Aida, M. S.; Attaf, N.; Zebbar, N. *Materials Science in Semiconductor Processing* **2015**, *30*, 645-650.
(55) Van der Wal, L. I. **2015**.
(56) Basirun, W.; Pletcher, D.; Saraby- Reintjes, A. *Journal of Applied Electrochemistry* **1996**, *26*, 873-880.
(57) Hernandez- Valdes, A.; Zarate, R. A.; Martinez, A. I.; Pech- Canul, M. I.; Garcia-Lobato, M. A.; Villaroel, R. *Vacuum* **2014**, *105*, 26-32.
(58) Navarro Yerga, R. M.; Galván, M. C. A.; del Valle, F.; Villoria de la Mano, J. A.; Fierro, J. L. G. **2009**, 471-485.
(59) Schoenmakers, J.
(60) Gregory, A. J.; Levason, W.; Noftle, R. E.; Penven, R. L.; Pletcher, D. **1995**, *399*, 415-420.
(61) Shannon, R. D.; Rogers, D. B.; Prewitt C.T. **1971**, *10*, 713-718.
(62) Kim, J. H.; Kim, J. H.; Jang, J. W.; Kim, J. Y.; Choi, S. H.; Magesh, G.; Lee, J.; Lee, J. S. *Advanced Energy Materials* **2015**, *5*, 1-9.
(63) Farhadian Azizi, K.; Bagheri- Mohagheghi, M. M. *Thin Solid Films* **2017**, *621*, 98-101.
(64) Chaudhary, Y. S.; Agrawal, A.; Shrivastav, R.; Satsangi, V. R.; Dass, S. *International Journal of Hydrogen Energy* **2004**, *29*, 131-134.
(65) Xu, Y.; Ao, Z. M.; Yuan, D. *Physics Letters A* **2012**, *376*, 2613-2616.
(66) Arca, E.; Fleischer, K.; Shvets, I. V. **2011**, 10-12.
(67) Berglund, S. P.; Abdi, F. F.; Bogdano, P.; Chemseddine, A.; Friedrich, D. **2016**.
(68) Liu, W. w.; Chen, H. x.; Liu, C. l.; Wang, R. *Physics Letters A* **2017**, *381*, 520-523.
(69) Filipovic, L. In *Topography Simulation of Novel Processing Techniques*, 2012; Chapter 4.1.2.
(70) Kose, S.; Atay, F.; Bilgin, V.; Akyuz, I. *Materials Chemistry and Physics* **2008**, *111*, 351-358.
(71) Liu, Y.; Gong, Y.; Mellott, N. P.; Wang, B.; Ye, H.; Wu, Y. *Science and Technology of Advanced Materials* **2016**, *17*, 1-10.
(72) Gregory, A. J.; Levason, W.; Pletcher, D. *Journal of Electroanalytical Chemistry* **1993**, *348*, 211-219.
(73) Barnabe, A.; Thimont, Y.; Lalanne, M.; Presmanes, L.; Tailhades, P. **2015**, 6012-6024.
(74) Yu, M.; Mcculloch, W. D.; Huang, Z.; Trang, B. B.; Lu, J.; Amine, K.; Yijing, W. *Journal of Materials Chemistry A: Materials for energy and sustainability* **2016**, *4*, 2766-2782.
(75) Suren, S.; Limkitnuwat, W.; Benjapongvimon, P.; Kheawhom, S. *Thin Solid Films* **2016**, *607*, 36-42.
(76) Levason, W.; Pletcher, D.; Smith, A. M. **1998**, *28*, 18-26.
(77) Gelderman, K.; Lee, L.; Donne, S. W. **2007**, *84*, 685-688.
(78) Manikandan, M.; Tanabe, T.; Li, P.; Ueda, S.; Ramesh, G. V.; Kodiyath, R.; Wang, J.; Hara, T.; Dakshanamoorthy, A.; Ishihara, S.; Ariga, K.; Ye, J.; Umezawa, N.; Abe, H. **2014**, 8-11.

(79) Muecke, U. P.; Messing, G. L.; Gauckler, L. J. *Thin Solid Films* **2009**, *517*, 1515-1521.
(80) Morales, J.; Sanchez, L.; Martin, F.; Ramos- Barrado, J. R.; Sanchez, M. *Electrochimica Acta* **2004**, *49*, 4589-4597.
(81) Abdelmounaïm, C.; Amara, Z.; Maha, A.; Mustapha, D. *Materials Science in Semiconductor Processing* **2016**, *43*, 214-221.
(82) Krol, R. V. D.; Grätzel, M., *Photo Electrochemical Hydrogen Production*, 2012, p 59.
(83) Gregory, A. J.; Levason, W.; Noftle, R. E.; LePenven, R.; Pletcher, D. *Journal of Electroanalytical Chemistry* **1995**, *399*, 105-113.
(84) Barnabé, A.; Thimont, Y.; Lalanne, M.; Presmanes, L.; Tailhades, P. *J. Mater. Chem. C* **2015**, *3*, 6012-6024.
(85) Perednis, D. *International Journal of Thin Films Science and Technology* **2003**.
(86) Rao, C. R.; Trivedi, D. C. *Coordination Chemistry Reviews* **2005**, *249*, 613-631.
(87) Chen, H. y.; Wu, J. h. *Applied Surface Science* **2012**, *258*, 4844-4847.

Appendices

Appendix A

Technical Developments

During the research some technological problems were resolved. The following sections will briefly address the problems and explain the technological developments.

A.1 Spray Pyrolysis

The spray pyrolysis set-up contains many different parts of which most were optimized, repaired or even replaced.

A.1.1 Heating Plate

Since spray pyrolysis is at high temperatures a high power heating plate is required. In order to keep heat loss and excessive heating of the complete set-up to a minimum the plate was partially insulated. As a result the temperature in the spray pyrolysis chamber decreased however, the plate itself and its electronics reached higher temperatures. Due to the excessive heating the electronic parts broke numerous times and had to be repaired. After several repairs the heating plate was damaged beyond repair and was replaced with a smaller, less powerful plate. The second heating plate required less insulation and therefore the electronics were more stable. However after two months the insulation of the heating element broke and caused a shot circuit. The heating plate was taken apart, new ceramic beads were installed and the delicate parts glued with ceramic glue. After the last repair the heating plate remained stable and worked properly throughout the rest of my thesis.

A.1.2 Atomizing Nozzle

Two different systems were tested, ultrasonic spray pyrolysis and air blast spray pyrolysis. The results of the USP nozzle were promising, however it broke down and was send for repair. During the months it was unavailable the air blast system was optimized for the blast results. The deposition setup itself is more cost efficient except for the duration since the deposition rate is lower and therefore depositing a film of similar thickness requires more time.

Figure A.1: Image of the cooling system constructed with peltier cells

A.1.3 Cooling system

A combination of the heat of the plate with the power of the ultrasonic nozzle caused the nozzle heat up quickly during spray pyrolysis. The changing temperature significantly affected the quality of the film and therefore a cooling system was required. In order to maintain a stable cooling rate throughout the reaction electric cooling was preferred over cooling with dry ice. A cooling system using peltier cells seemed ideal since it quickly cools to $-5\,°C$. A peltier cell uses small bandgap semiconductors to transfer heat from side to side. One face of the peltier will be heated to $60\,°C$ while the other is cooled to $-5\,°C$. In order to further improve cooling the heat from the warm face needs to be dissipated to air. Large radiators combined with $12\,V$ ventilators were implemented for an efficient heat transfer. Similarly the cold face was attached to another radiator through which air or nitrogen was blown. The cooled stream could be used directly as carrier gas or as cooling for the nozzle. Figures A.1 and A.2 show the final version of the cooling system which was able to efficiently cool air to freezing temperatures.

A.2 Photo Electrochemical Setup

Photo electrochemical measurements need to be performed in a black box to ensure a similar light intensity between measurements. During the thesis a black box setup was present untill it was taken apart to build a new solar simulator. In order to keep doing experiments using the old a setup a new black was required. The technical staff was flooded with other tasks and therefore I decided to build the setup myself. Below are two image, figure A.4 and A.3, showing the new black box

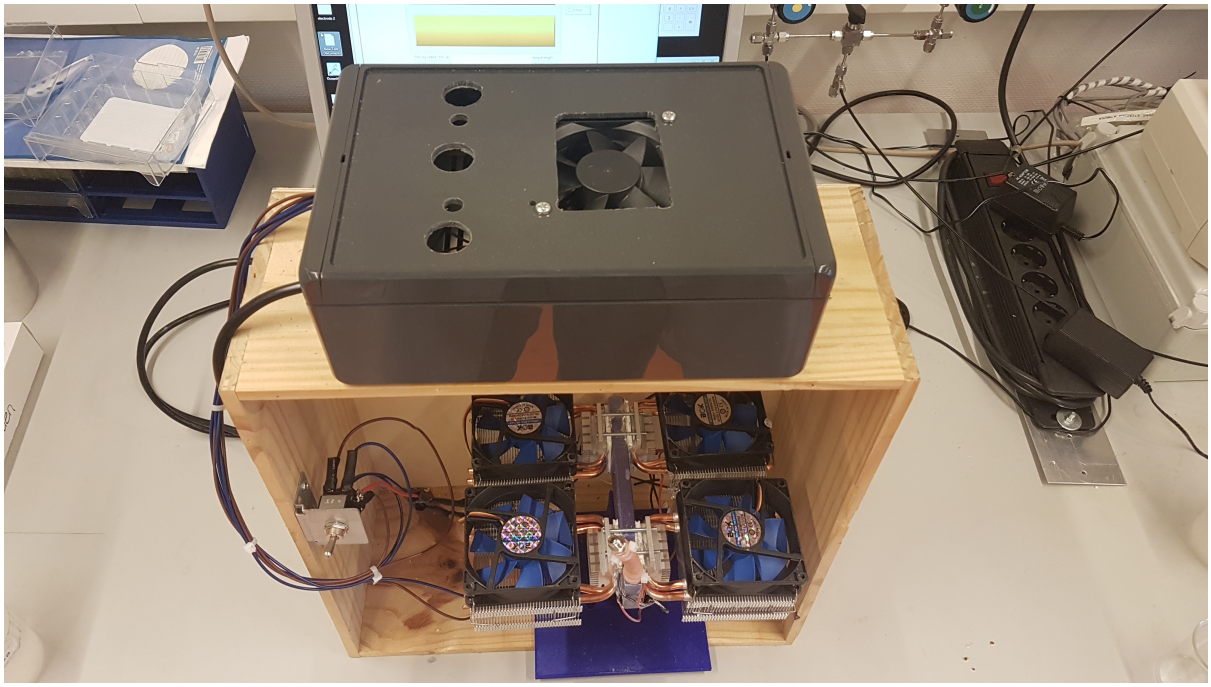

Figure A.2: Image of the cooling system showing the radiator, peltier cells and power supply

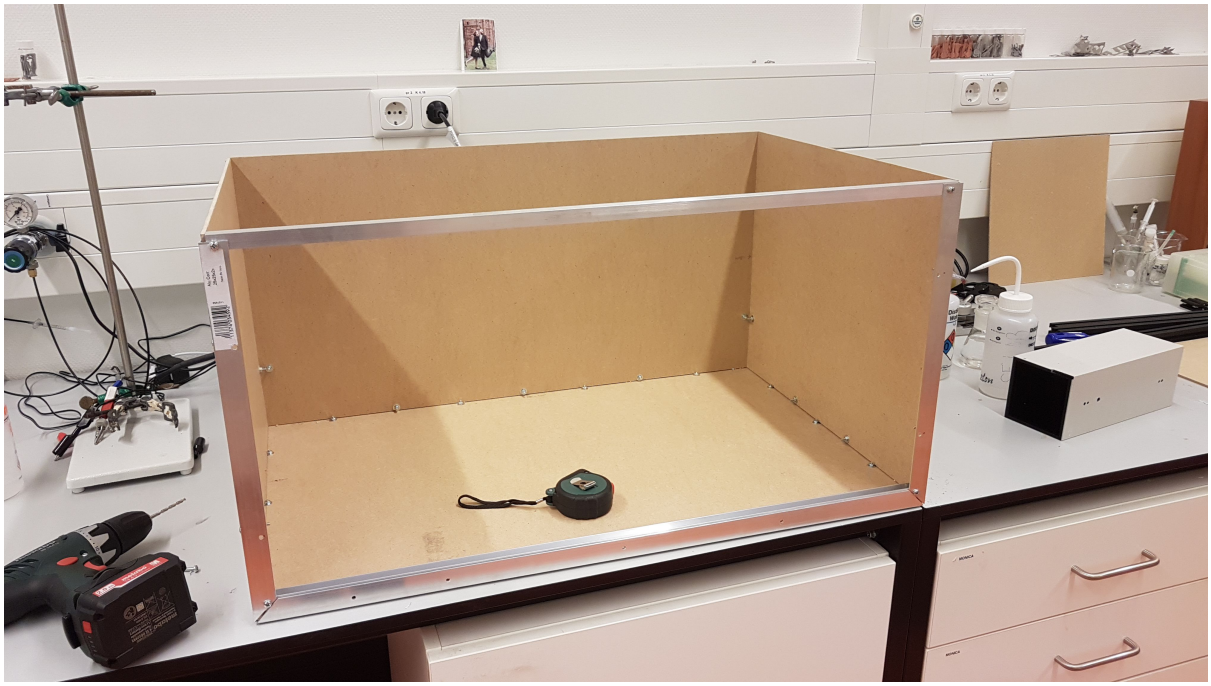

Figure A.3: Image of the blackbox of the photo electrochemical set up during construction

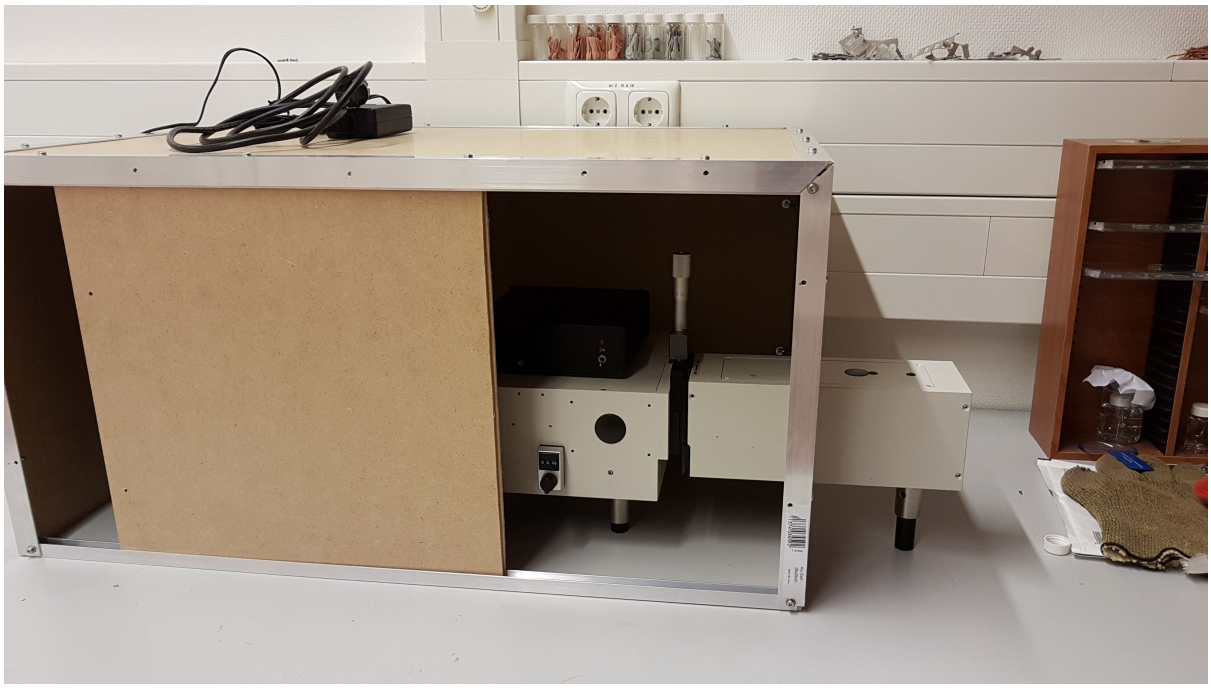

Figure A.4: Image of the final electrochemical set up containing the lamp, a monochromator, beam chopper and the Teflon electrochemical cell

Appendix B

Thermogravic analysis

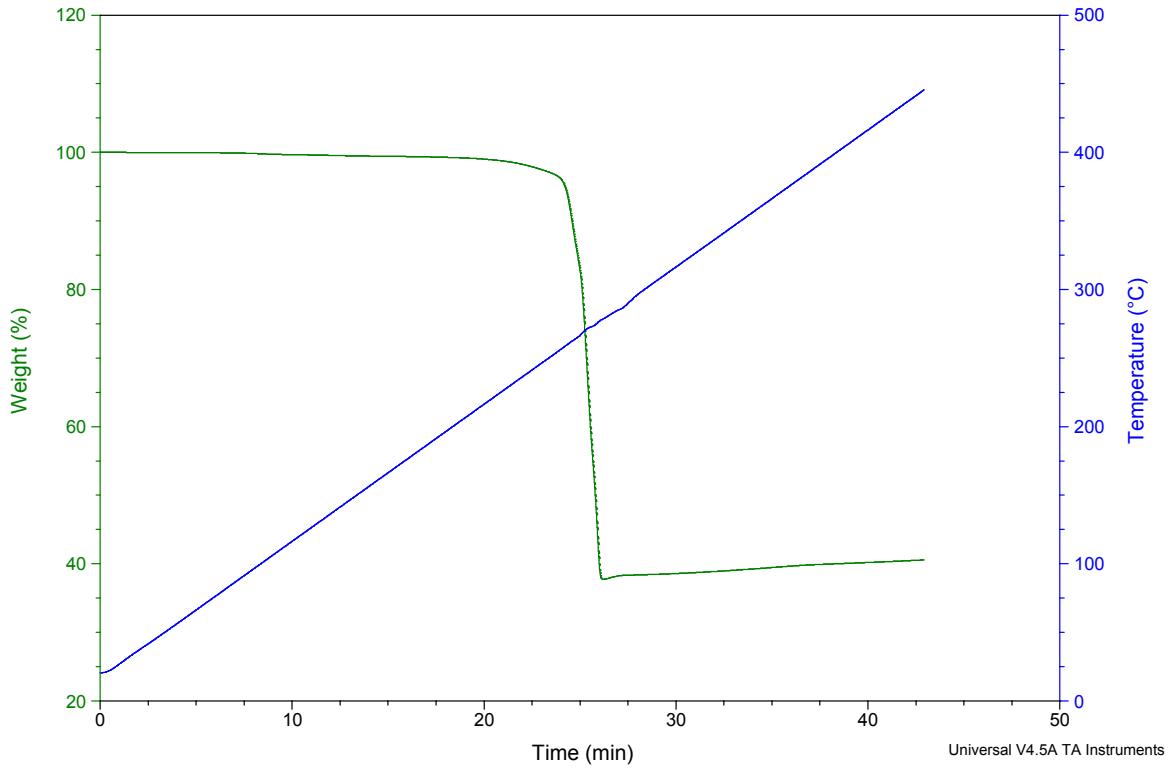

Figure B.1: Thermogravimetric analysis of copper acetate showing the weight in percentage, time and temperature. A linear heating ramp can be observed confirming the heating ramp of $10\,^{\circ}\mathrm{C}\,\mathrm{s}^{-1}$. A reduction in weight is observed at approximately 300 °C which is ascribed to the decomposition of copper acetate.

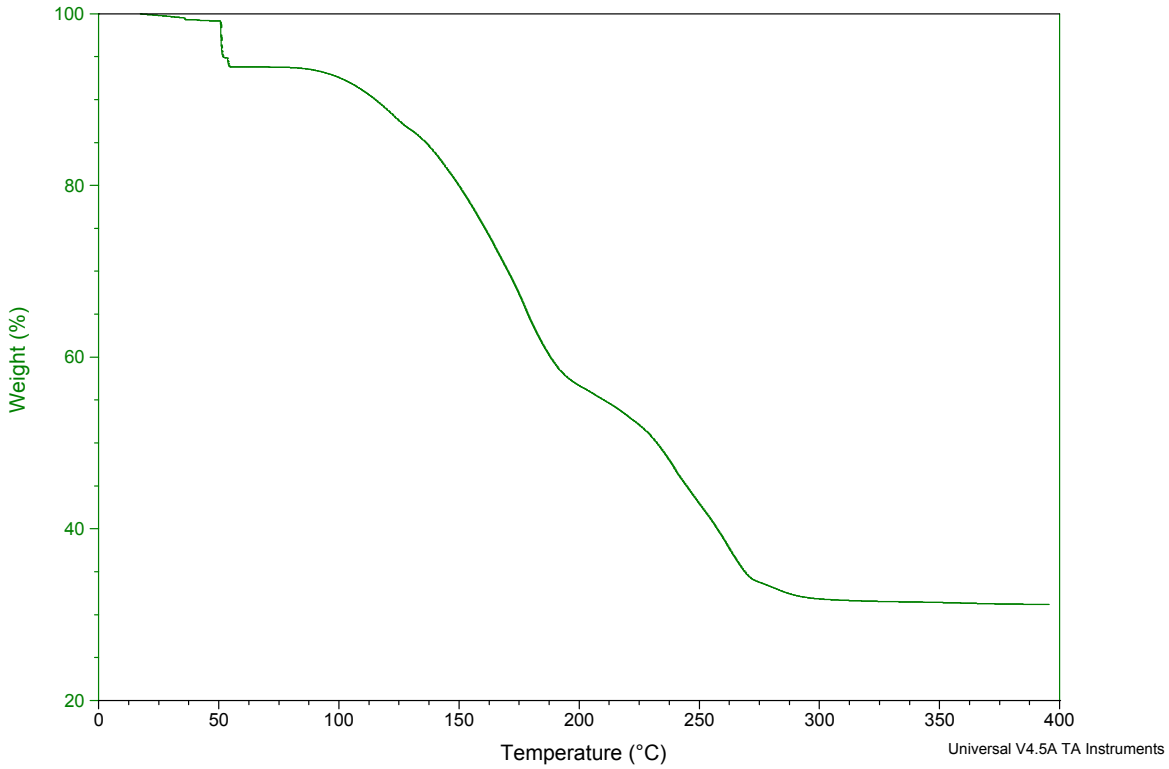

Figure B.2: Thermogravimetric analysis of $Cu(NO_3)_2 \cdot 3\,H_2O$ showing an initial weight reduction below 100 °C which is believed to be excess water. Further regimes are ascribed to a stepwise loss of hydrates combined with the decomposition of the nitrate. A full decomposition is reached at 300 °C.

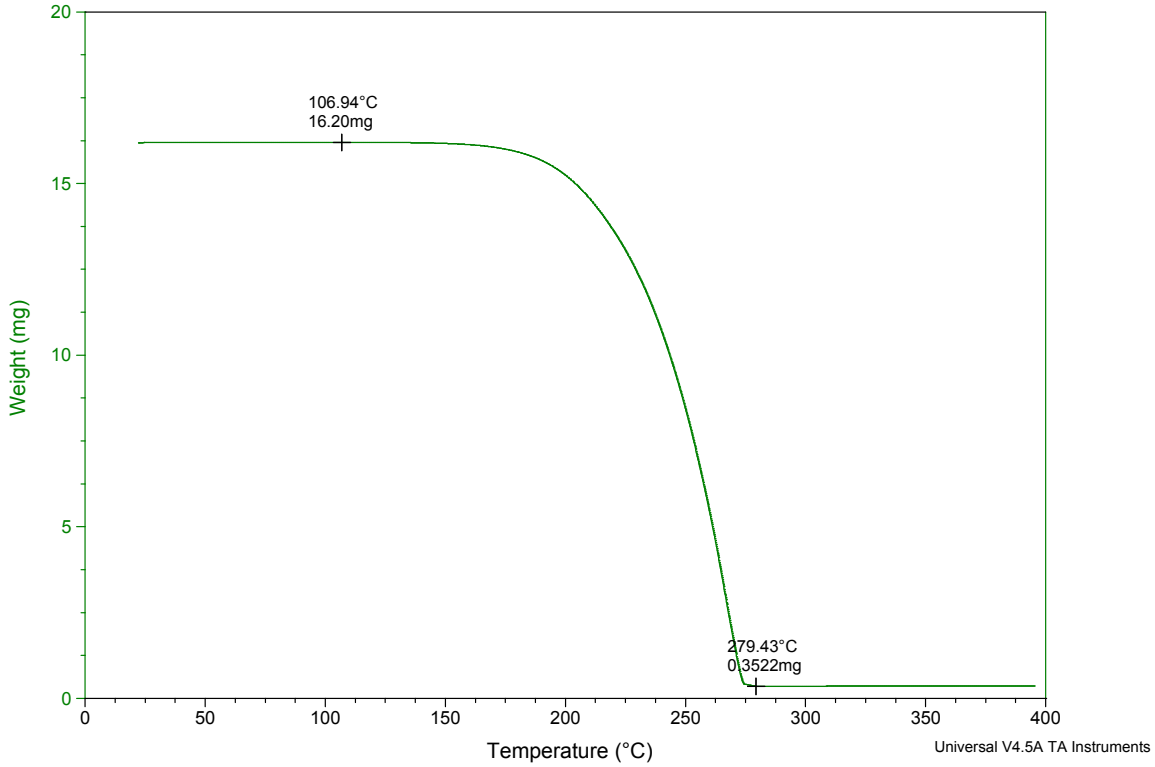

Figure B.3: Thermogravimetric analysis of copper acetylacetonate showing a deposition pathway from 175 °C to 275 °C.

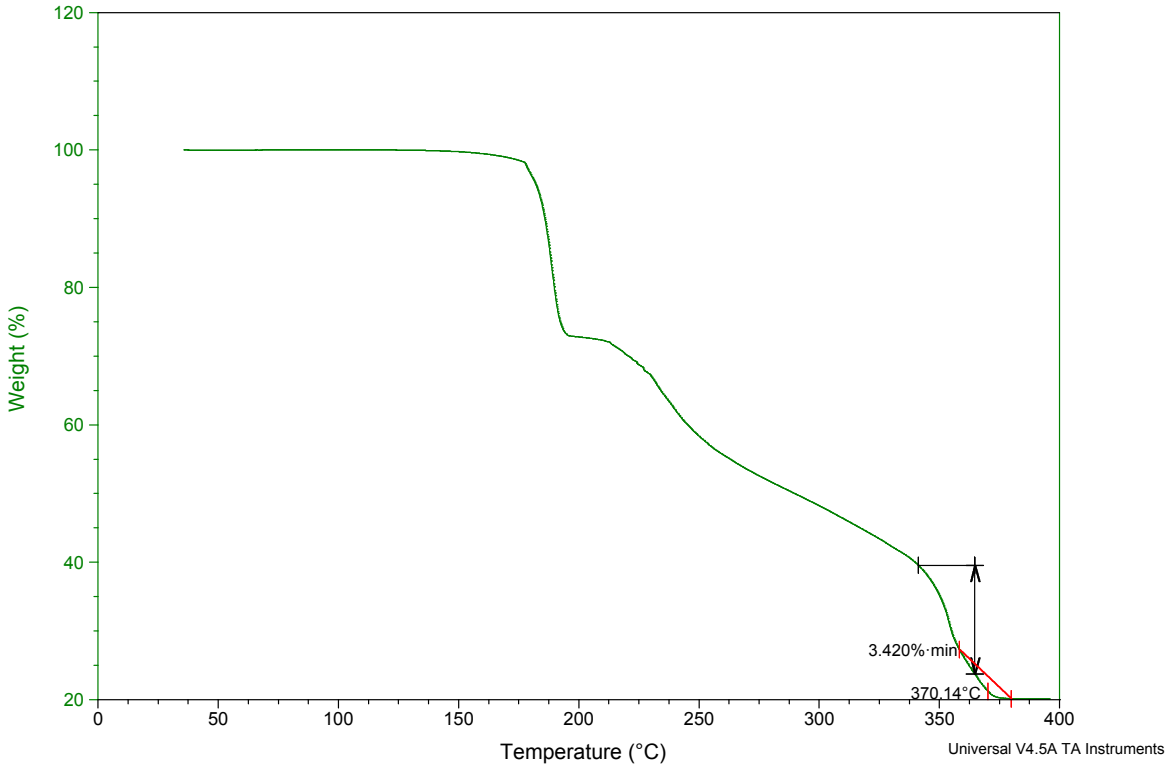

Figure B.4: Thermogravimetric analysis of iron acetylacetonate showing various decomposition steps and a full decomposition is reached at 375 °C.

Appendix C

Catalyst deposition

Catalyst deposition was briefly tested however, proved to be more difficult than expected and was there postponed to a next project. Underneath a brief summary of the examined methods.

C.1 Method one

Different catalysts were deposited on the resulting delafossite $CuFeO_2$ thin films using photo-electrochemical deposition. A 200 mM solution of sodium phosphate was used as a buffer solution and 5 mM of platinum was added. The samples were placed in a teflon cell containing the deposition solution. A continuous beam of solar light was created using the xenon lamp and used to illuminate the sample within the deposition solution. A cyclic voltametry was performed from 1.0 V to 0.4 V vs RHE for 60 cycles. Using this method the platinum was deposited on the most active sites.

C.2 Method two

In collabaration with Jochem Wijten (MSc) a nickel/molydenum hydrogen evolution catalyst was deposited. A plating bath containing high concentrations of both nickel and molybdenum precursor together with a phosphate buffer was deposition using a chronopotentionometry using a stable current of 10mA.

C.3 Method three

An organic platinum precursor was painted on the delafossite $CuFeO_2$ photocathodes. The catalyst was dried at 100 °C for one hour and afterwards annealed various temperatures ranging from 300 °C to 400 °C for one to two hours.

C.4 Result

Getting conclusive results of any of the catalyst depositions turned out to be challenging and required more research. Method one and two both electrodeposition have potential and should be further investigated. However, method three lead to oxidation of the copper iron oxide which then lead to degradation of the sample during photoelectrochemical testing.